

# Fundamentals of underwater acoustics

---

T.G. LEIGHTON

## 7.1 INTRODUCTION

The topic of underwater acoustics has traditionally concentrated on ocean acoustics, with the emphasis on sonar. This field is covered by a chapter in the companion volume to this book, and by a number of texts (Tolstoy and Clay, 1966; Albers, 1972; Ross, 1976; Clay and Medwin, 1977; Kinsler *et al.*, 1982; Urick, 1983; Burdick, 1984; Coates, 1990). Therefore this chapter, rather than reiterating this material, will cover the principles underlying sound transmission through water by relating main themes common to diverse applications of underwater sound. The progression of ideas is outlined in Fig. 7.1.

Following this introduction, the chapter is divided into three sections, as shown in the figure. Section 7.2 examines the basics of sound propagation in water, as predicted by linear acoustics, recalling the dependence of the sound speed on the density and bulk modulus of the liquid. Specifically, the section opens with an examination of how this dependence affects ocean acoustics, through the variation of the sound speed with hydrostatic pressure, temperature, salinity and bubble presence. This leads to a discussion of sound speed variation with depth, and how this so-called 'sound speed profile' varies with latitude, season and meteorological conditions. There follow descriptions of how the characteristics of such profiles can lead to the formation of oceanic sound channels, and how propagation over long ranges in such channels is influenced by attenuation from both geometrical spreading and acoustic absorption. Since past exploitation of such channels has been extensively covered in the above references, the text is then restricted to a more recent application of such channels, namely acoustic thermometry of the ocean climate.

Key to the long-range propagation exploited in acoustic thermometry is the signal-to-noise ratio and, through examination of ambient noise, other

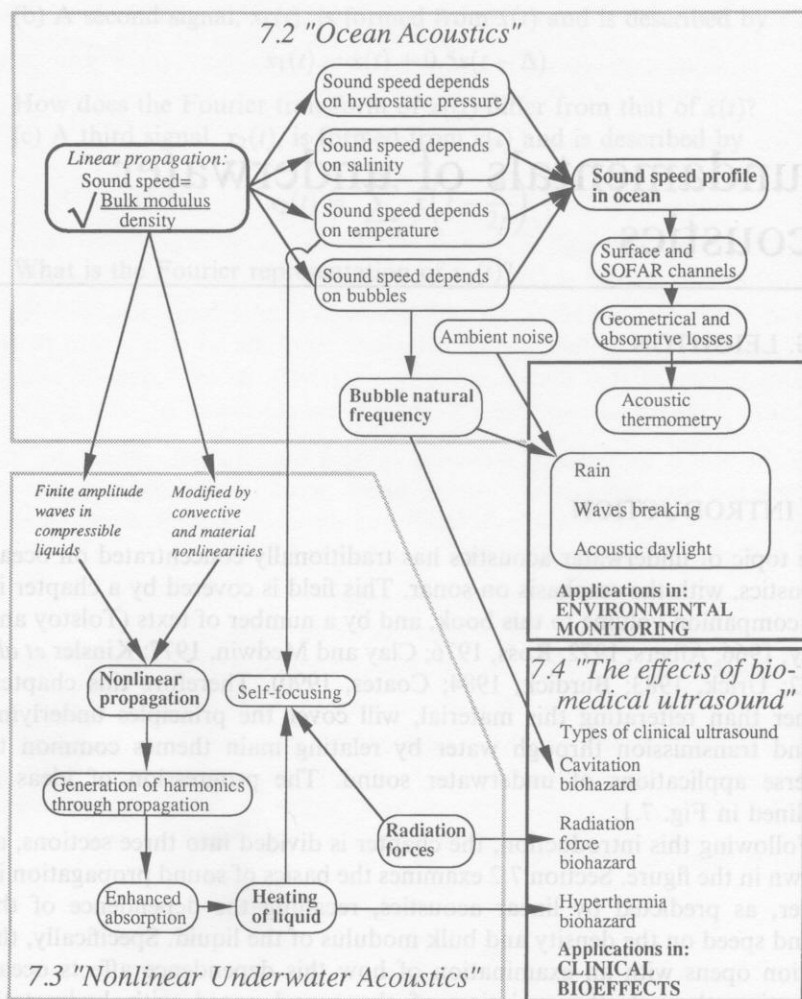


**Figure 7.1** Schematic of the progression of ideas through the chapter, showing conceptual links. The titles of the boxes for sections 7.2, 7.3, and 7.4 are given. The course begins in the top left-hand of the figure.

techniques for environmental monitoring using underwater acoustics are then described. This is done through expansion of the topic of bubble acoustics, introduced earlier through their effect on the sound speed. The text outlines how the sound emissions generated by bubbles on entrainment give information about rainfall over the ocean, and about wave breaking (which, in turn, relate to the fluxes of mass, momentum and energy between

the atmosphere and the ocean). Other sources of ambient noise, and their roles in the exploration of the oceans, are then described.

Section 7.3 of the text describes the nonlinear propagation of finite amplitude sound. Nonlinear propagation is compared with the linear model which was discussed thoroughly in Chapter 1, and there follows a description of key consequences (the generation of harmonics and shocks, self-focusing, enhanced heating of the liquid and radiation force effects). These effects, and the potential for cavitation, are combined in section 7.4 in a discussion of the possibility of ultrasonic bioeffects, which may be required in therapy but unwanted when diagnostic ultrasound is used.

By examining the subject through the underlying physics, diverse applications (and their similarities) are illustrated. The range encompasses clinical effects on the sub-millimetre scale and, at the other extreme, propagation paths of order 1000 km in studies of ocean climate. The latter application illustrates how today the use of sound to probe the oceans can involve the dedication of huge resources (staff, finance, equipment, etc.). Indeed in the years following the Second World War, the investment in underwater acoustics has increased possibly more than in any other branch of acoustics. It is perhaps ironic that in advancing from simple sound speed measurements in 1827 using an underwater sound source (a bell) and a reference in-air electromagnetic wave (light), through the use of underwater acoustics in navigation, detection and exploration, the ocean basin-scale experiments conducted today bear strong similarities with that early experiment, and the same physics links both with applications of medical ultrasound.

## 7.2 OCEAN ACOUSTICS

### 7.2.1 History

The history of underwater acoustics is presented in detail in the references cited at the start of this chapter, and therefore only a brief outline is given here. In 1490 Leonardo da Vinci wrote: 'If you cause your ship to stop, and place the head of a long tube in the water and place the outer extremity in your ear, you will hear ships at a great distance from you.' This early statement contained features still important today in the use of passive sonar, da Vinci drawing attention to the following requirements: low self-noise, acoustic coupling to overcome impedance mismatch, a receiver transducer, and a recognition system. This system was used as late as the First World War, when directivity was gained by the employment of a second tube.

As will be seen shortly, of key importance to ocean acoustics is the sound speed in the water. The first measurements of this were made in 1827 in Lake Geneva/Leman by Daniel Colladon, a Swiss physicist, and Charles François

Sturm, a French mathematician. From the time interval between the observation of a flash of light and the sound from an underwater bell, both signals having been generated simultaneously, they calculated the speed of sound in the lake to be 1435 m/s. The water temperature was 8 °C. By the end of that century, knowledge of the sound speed in water allowed the exploitation of such signals in navigation. Figure 7.2 shows schematically how, from the time-interval  $t_1$  between hearing a foghorn and an underwater bell (both sounded simultaneously on a lightship at time  $t = 0$ ), the distance  $X$  of the observer to the lightship could be calculated. The speeds of sound in air,  $c_a$ , and water,  $c_w$ , are known, and the interval  $t_1$  is measured. If the underwater signal takes time  $t_0$  to reach the observer, then the air signal takes time  $t_0 + t_1$ , and

$$X = c_w t_0 = c_a t_0 + c_a t_1 \quad (7.1)$$

implying

$$t_0 = \frac{c_a t_1}{(c_w - c_a)} \quad (7.2)$$

and

$$X = \frac{c_w c_a t_1}{(c_w - c_a)} \quad (7.3)$$

Significant advances followed once transducers were introduced to interconvert electrical and mechanical signals. The piezoelectric effect was discovered in 1880 by Pierre and Jacques Curie, who noted that electric charges appear on faces of certain stressed crystals. The effect is reversible, and therefore can be exploited in both transmitters and receivers, ceramics and polymers often being used nowadays in preference to crystals. Also reversible is the magnetostrictive effect, discovered by James Joule in around 1840, who observed that certain materials change length in a magnetic field.

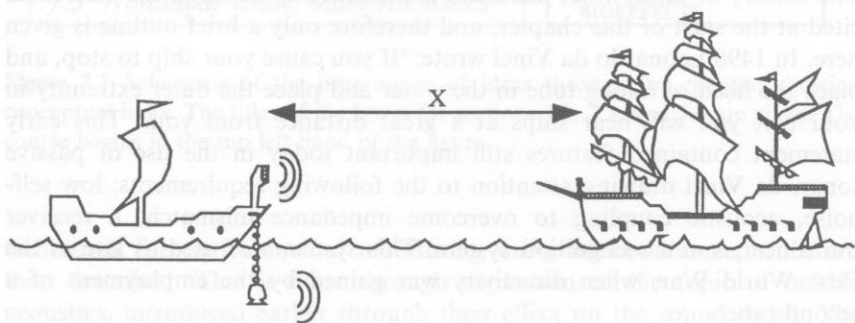


**Figure 7.2** Schematic of use of airborne and underwater sound to determine distance to a lightship.



The use of alternating electric and magnetic fields can therefore be exploited to generate acoustic waves of a specific spectral content. Significant advances took place in the first half of this century, due in considerable part to the world wars, such that acoustic techniques, including sonar (retrospectively an acronym for 'sound navigation and ranging') represent probably the most powerful way of exploring the oceans. An example of passive sonar was described above, in da Vinci's description of listening for ships. An example of active sonar, where the scattering of an acoustic pulse previously transmitted by the detecting agent gives the range (from the travel time) and direction (from the directionality of the transmitter and/or receiver), is shown schematically in Fig. 7.3.

The transmission of an acoustic signal and the subsequent location of a target through detection of the acoustic reflections from it (echo-location) is a technique used by many mammals. Bats employ frequencies  $f$  in the range 30 kHz to 80 kHz, while toothed whales use frequencies up to 200 kHz (Leighton, 1994). One reason for the difference is that the speed of sound in water is roughly five times that in air, and so to obtain the same degree of spatial resolution higher frequencies must be employed in water. In echo-location, the limit of spatial resolution is roughly given by the size of the wavelength used, as illustrated by a simple estimation from the phase speed,  $c_0$ , of the wavelength,  $\lambda$ . The speed of sound in air at 20 °C and under one atmosphere of pressure is 343 m/s. Since  $c_0 = f\lambda$  (see section 1.1 of Chapter 1), the wavelength at 80 kHz is 4.3 mm, indicating that bats can echo-locate objects down to a few mm size, corresponding to their diet of insects. Interestingly, those bats which eat fruit rather than insects tend not to use echo-location but instead find their larger, stationary food by sight. The speed of sound in water is roughly 1480 m/s, and so at 80 kHz the wavelength is nearly 2 cm. To achieve a similar degree of spatial resolution as bats, toothed whales must exploit higher frequencies; at 200 kHz, the

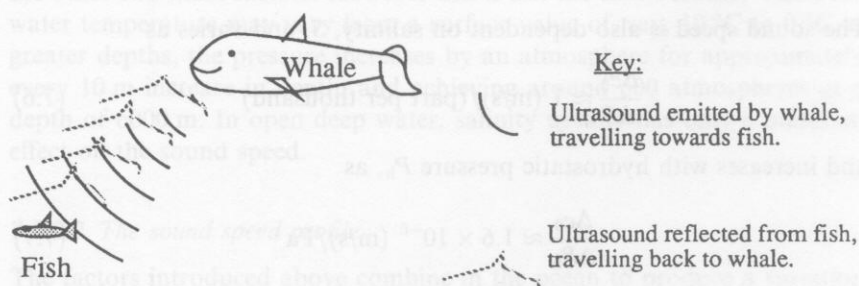


**Figure 7.3** Schematic illustration of active sonar. The example illustrates monostatic active sonar, where the source and receiver are located at the same position; with bistatic sonar they are not.

maximum frequency toothed whales exploit, the wavelength in water is around 7 mm.

## 7.2.2 The speed of sound

### 7.2.2.1 The factors affecting the oceanic sound speed

From section 1.3 of Chapter 1, it is clear that a model of linear acoustic propagation demonstrates that the sound speed,  $c_0$ , depends on the equilibrium density,  $\rho_0$  of a liquid, and on the bulk modulus,  $K$ . For a fixed mass of fluid, the bulk modulus equals  $K = dP/(d\rho/\rho) = -dP/(dV/V)$  (where  $P$  is the total fluid pressure and  $dV/V$  the proportional change in volume of a fluid element). Specifically,

$$c_0 = \sqrt{\frac{K}{\rho_0}} \quad (7.4)$$

In seawater, this dependence is not simple. The temperature-dependent nature of even pure water is, for example, anomalous in that it achieves maximum density at 4 °C. It is, however, anomalous in other ways. There is a strong dependency of the sound speed in water on temperature, as shown in Fig. 7.4 for pure water under one atmosphere of pressure. In many liquids, the sound speed decreases with increasing temperature, but water is anomalous in that it reaches a maximum (at 74 °C for pure water under one atmosphere), and in the temperature range of the ocean the sound speed increases with increasing temperature,  $T$ . The magnitude of the effect in the ocean is

$$\frac{\Delta c_0}{\Delta T} \approx 5 \text{ (m/s)/}^\circ\text{C} \quad (7.5)$$

The sound speed is also dependent on salinity,  $S$ , and varies as

$$\frac{\Delta c_0}{\Delta S} \approx 1 \text{ (m/s)/(part per thousand)} \quad (7.6)$$

and increases with hydrostatic pressure  $P_h$ , as

$$\frac{\Delta c_0}{\Delta P_h} \approx 1.6 \times 10^{-6} \text{ (m/s)/Pa} \quad (7.7)$$

(Urick, 1983; Del Grosso, 1974). (These relations are given in the references in non-S.I. units. Differentiation of equation (7.8) will yield such results.) The sound speed in the ocean depends on a range of other phenomena, notably the subsurface bubble layer if one exists (section 7.2.2.5(b)).

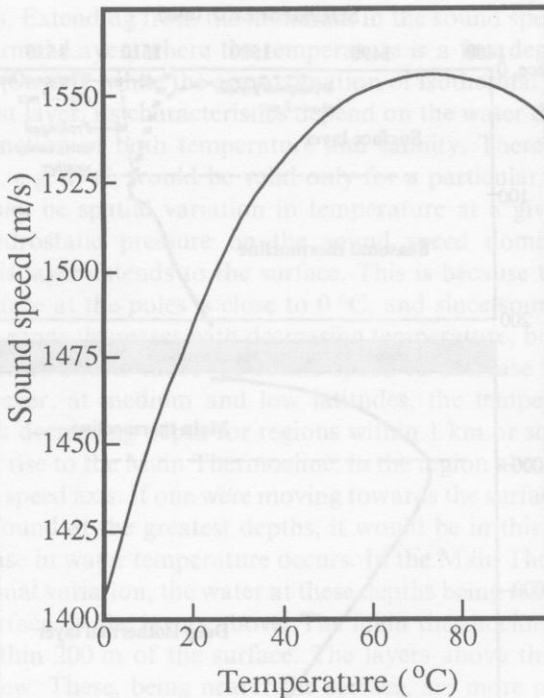


**Figure 7.4** The temperature variation of the speed of sound in pure water, for linear propagation under one atmosphere of pressure. (Reprinted Leighton (1994) by permission of the publishers, Academic Press, London.)

At first sight equations (7.5) to (7.7) may give the impression that the hydrostatic pressure has only a minor effect on the sound speed compared to the other two main factors. However this is not the case because, whilst the water temperature may vary from a surface value of, say, 10 °C to 0 °C at greater depths, the pressure increases by an atmosphere for approximately every 10 m increase in depth, and achieving around 600 atmospheres at a depth of 6000 m. In open deep water, salinity usually has only a marginal effect on the sound speed.

#### 7.2.2.2 The sound speed profile

The factors introduced above combine in the ocean to produce a variation of sound speed with depth known as the sound speed profile. A typical example is shown in Fig. 7.5. The profile allows division of such an oceanic section into characteristic regions. Consider that area of the figure which portrays the ocean at depths of greater than 200 m. This area comprises two

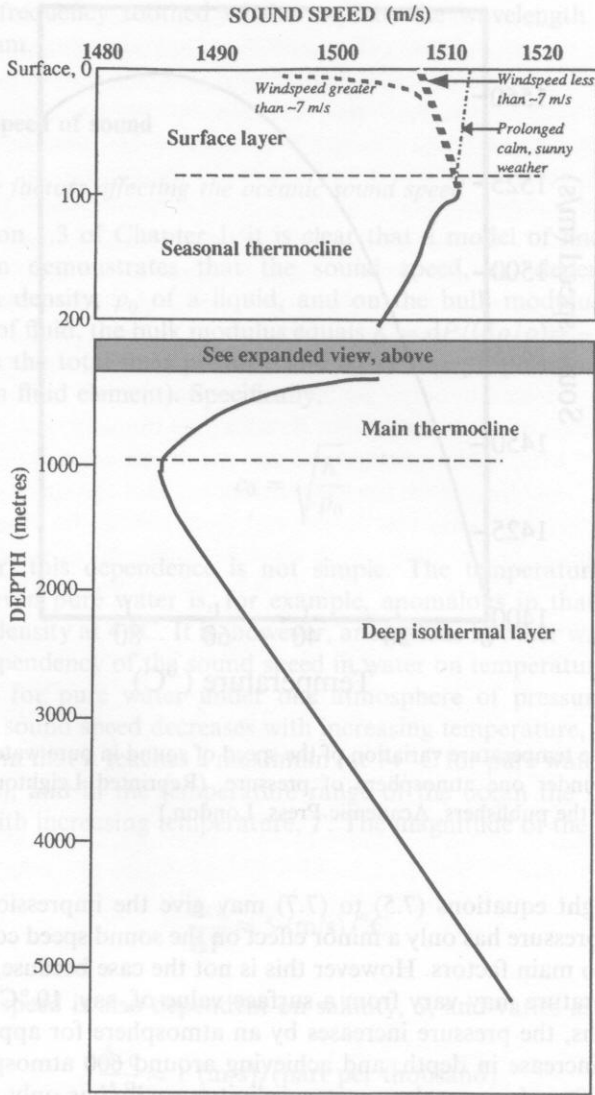


**Figure 7.5** A typical sound speed profile. The upper 200 m are shown in magnification. In the surface layer, three possible sound speed profiles are shown, corresponding to the following wind conditions: prolonged calm, sunny weather (dot-dash line); a windspeed less than about 7 m/s (thin dashed line); windspeed in excess of about 7 m/s (thick dashed line).

main regions. Extending from the minimum in the sound speed profile is the Deep Isothermal Layer, where the temperature is a few degrees centigrade above  $0^{\circ}\text{C}$ . (Strictly, while the approximation of isothermal may be applied to the deepest layer, its characteristics depend on the water density, which is in turn a function of both temperature and salinity. Therefore any stated temperature, e.g.  $4^{\circ}\text{C}$ , would be valid only for a particular salinity, and in fact there may be spatial variation in temperature at a given depth.) The effect of hydrostatic pressure on the sound speed dominates. At high latitudes, this layer extends to the surface. This is because the temperature near the surface at the poles is close to  $0^{\circ}\text{C}$ , and since sound speed in this temperature range decreases with decreasing temperature, both the pressure and temperature effects cause the sound speed to decrease with decreasing depth. However, at medium and low latitudes, the temperature tends to increase with decreasing depth for regions within 1 km or so of the surface.

This gives rise to the Main Thermocline, in the region above the minimum in the sound speed axis. If one were moving towards the surface from the very cold water found at the greatest depths, it would be in this region that the major increase in water temperature occurs. In the Main Thermocline, there is little seasonal variation, the water at these depths being relatively insulated from the surface by the layers above. The main thermocline extends in the figure to within 200 m of the surface. The layers above this are shown in expanded view. These, being nearer the surface, are more prone to surface influence (seasonal, and, in the shallower waters, meteorological, effects).

In the Seasonal Thermocline, the temperature decreases with depth. This region is well-defined in summer and autumn. During winter and spring, and in the Arctic, it merges with surface layer. The reason is that a well-defined thermocline needs a strong temperature gradient, which requires high temperatures near the surface since the depths are thermally more stable and cold. In the Arctic, the surface is always cold, so the thermocline is weak. Elsewhere, this situation holds in winter and spring because the sea is slow to warm up and to cool down.


Nearest the surface (0–100 m depth in the figure) is the Surface Layer, which is subject to daily and local changes, wind, and temperature. If it has been calm and sunny for long periods, the temperature decreases with depth in this region, and the thermocline extends to the surface (see the dot-dash line in the figure). However this layer may be mixed up by wind and circulations so that it becomes isothermal (hence the alternative name of this region is the Mixed Layer). If windspeed is  $> 7\text{ m/s}$ , bubbles dominate in the upper 10 m or so and reduce the sound speed drastically. Two dashed lines are shown in the figure. The thick one (on the right) shows a steady decrease in sound speed resulting from a pressure effect in an isothermal surface layer that has been mixed up by low windspeeds (below  $7\text{ m/s}$ , say  $3\text{ m/s}$ ). The thin dashed line (on the left) shows a marked decrease in sound speed, relevant to wind speeds in excess of  $7\text{ m/s}$  (say,  $10\text{ m/s}$ ), resulting from



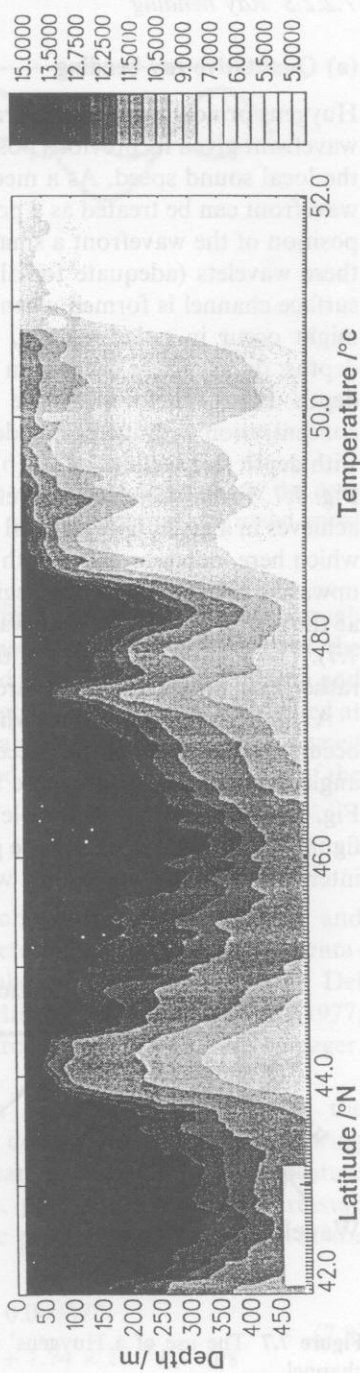
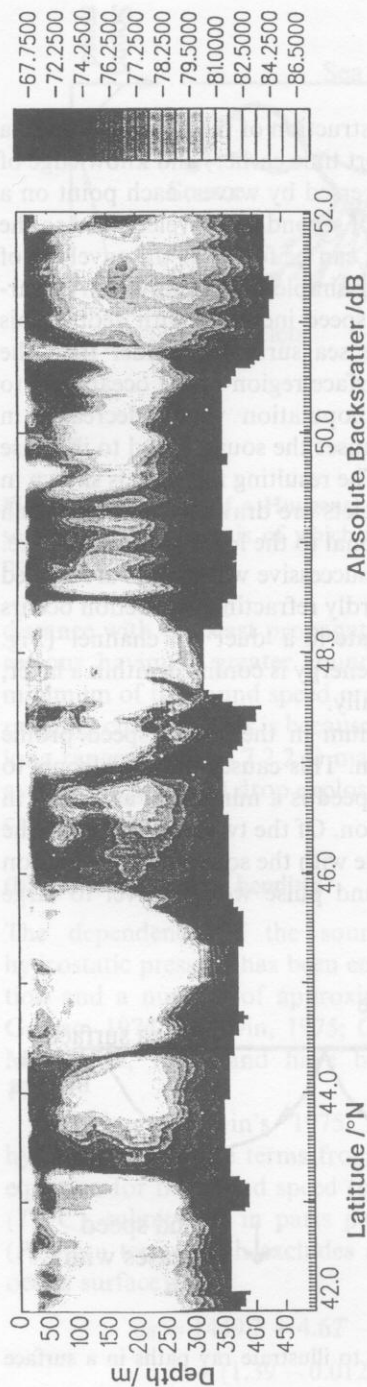
bubble entrainment. It should however be noted that the influence of the bubbles on the sound speed will be dependent on the acoustic frequency – see section 7.2.2.5(b).

The sound speed profile shown in Fig. 7.5 reflects the body of information which has been gathered over the years through submerged sensor measurements. However, such surveying is costly and the profile will vary both in time and in the horizontal plane since, for example, temperature and salinity may do so. Figure 7.6 shows concurrent sections from cruise 59 of the research vessel *Charles Darwin* showing, against a common latitude scale, measurements of the temperature and of the acoustic backscatter (from zooplankton) obtained from a 150 kHz Acoustic Doppler Current Profiler (ADCP). The transect of this region of the NE Atlantic took four days, and so shows two normal daily migrations of zooplankton at around 44° and 46° latitude, a behaviour which is interrupted by the Polar Front at around 49° (visible on the thermal record).

The figure shows how the ocean contains many features on the mesoscale (approximately 100 km) order. These can be thought of as being the equivalent of features (e.g. depressions and anticyclones, fronts etc.) which can be observed on weather maps. However the size scale of such features tends to be an order of magnitude smaller in the ocean (e.g. eddies have 100 km width, as opposed to 1000 km width), although the inertia and heat capacities associated with such features in the ocean are vastly greater than those observed in the atmosphere. Eddy features have been reviewed by Robinson (1983). Currents representing the motion of millions of tonnes of water exist, and these have significance to climate and ocean transport (Wunsch, 1981). The interaction between currents and land masses (e.g. Cape Horn) represent one source of eddies, and large-scale flows such as the Gulf Stream can be a significant source. Examination of such behaviour has been facilitated by the development of high-resolution model simulations of ocean circulation (Webb *et al.*, 1991). Timescale variability is in terms of days to months. In fact, inhomogeneities in ocean parameters occur right across the dimension scale, from basin-scale (of a dimension similar to, for example, the Atlantic or Pacific basins) to micro-scale. Small-scale circulations and turbulence can have sub-metre and sub-second scales. One source of sound speed variation on such a scale, wave-entrained bubbles, is discussed in section 7.2.2.5(c).



**Figure 7.6** Concurrent sections from a cruise showing, as a function of latitude and depth, the temperature and the absolute acoustic backscatter obtained from a 150 kHz Acoustic Doppler Current Profiler (ADCP). The backscatter is referenced to the scattering cross-section of  $1 \text{ m}^2$  (square) of target per  $1 \text{ m}^3$  (cube) of water. Supplied by kind permission of H. Roe.



## 7.2.2.3 Ray bending

## (a) Qualitative ray bending

Huygens principle allows the graphical construction of the new position of a wavefront given its previous position (a short time earlier) and knowledge of the local sound speed. As a medium is traversed by waves, each point on a wavefront can be treated as a point source of secondary wavelets, and so the position of the wavefront a small time later can be found as the envelope of these wavelets (adequate for all manner of simple, linear waves). A near-surface channel is formed when the sound speed increases with depth. This might occur in polar regions, because the sea surface is colder than the depths; or elsewhere because in the near-surface region of the ocean (say to depth 10 m), there might be a bubble population which decreases in concentration with increasing depth, and causes the sound speed to increase with depth (see section 7.2.2.5(b) and (c)). The resulting ray path is shown in Fig. 7.7. From successive wavefronts, wavelets are drawn. The radius each achieves in a given time interval is proportional to the local sound speed (i.e. which here increases with depth). As such, successive wavefronts are angled upwards, indicating that the region is upwardly refracting. Reflection occurs at the sea surface, such that waves propagate in a 'duct' or 'channel' (Fig. 7.7). The result is that much of the acoustic energy is confined within a layer, rather than spreading in all directions equally.

A similar effect is found when a minimum in the sound speed profile occurs, as discussed in the preceding section. This causes the wavefronts to angle towards the depth where the sound speed is a minimum, as shown in Fig. 7.8 using a Huygens wavelet construction. Of the two rays shown in the figure, the one which makes the greater angle with the sound channel axis on intersection is the one along which a sound pulse would travel to large

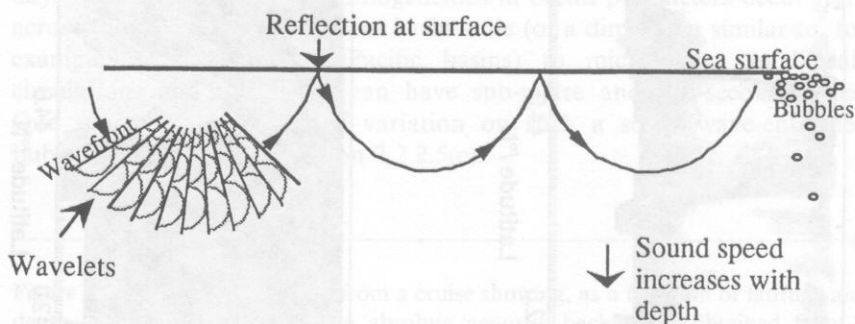


**Figure 7.7** The use of a Huygens' construction to illustrate ray paths in a surface channel.

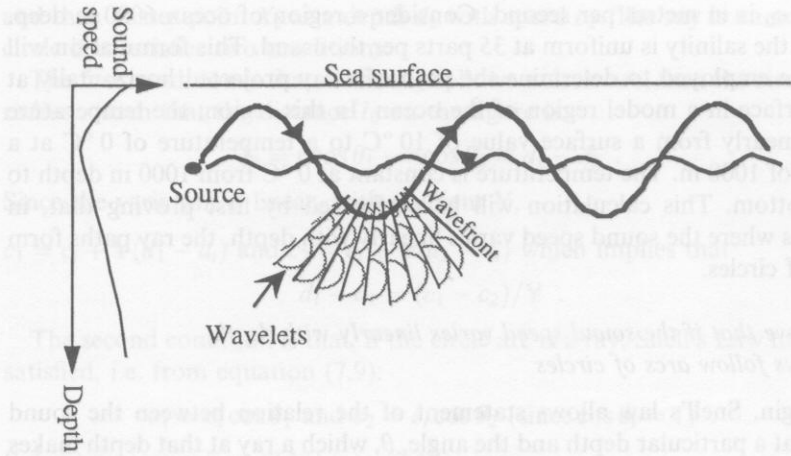


**Figure 7.8** The use of a Huygens' construction to illustrate ray paths in the deep sound channel, the axis of which is located at the minimum in the sound speed profile.

distance with the least propagation time. This is because it travels through regions having a greater sound speed. The channel which forms at the minimum of the sound speed profile is called the SOFAR (sound fixing and ranging) channel. This is because acoustic signals within it can be detected at long ranges (section 7.2.2.4) making it suitable for use in locating downed aviators (who might drop explosives designed to detonate at the depth of the channel axis).

### (b) Quantitative ray bending

The dependence of the sound speed on temperature, salinity, and hydrostatic pressure has been empirically determined through experimentation and a number of approximate formulations exist (Leroy, 1969; Del Grosso, 1974; Medwin, 1975; Chen and Millero, 1976; Chen *et al.*, 1977; Mackenzie, 1981) and have been compared (Spiesberger and Metzger, 1991).

Adapting Medwin's 1975 formulation to separate specifically the hydrostatic pressure terms from the depth dependence gives the following equation for the sound speed ( $c$ ) in the ocean as a function of temperature ( $T/^{\circ}\text{C}$ ), salinity ( $S$ , in parts per thousand, ppt) and hydrostatic pressure ( $P_h/P_a$ , a term which excludes atmospheric pressure and so is zero at the ocean surface):

$$c_0 = 1449.2 + 4.6T - 0.055T^2 + 0.0003T^3 \\ + (1.39 - 0.012T)(S - 35) + 1.74 \times 10^{-6}P_h \text{ m/s} \quad (7.8)$$

where  $c_0$  is in metres per second. Consider a region of ocean 6000 m deep, where the salinity is uniform at 35 parts per thousand. This formulation will now be employed to determine the path of a ray projected horizontally at the surface in a model region of the ocean. In this region, the temperature falls linearly from a surface value of  $10^\circ\text{C}$  to a temperature of  $0^\circ\text{C}$  at a depth of 1000 m. The temperature is constant at  $0^\circ\text{C}$  from 1000 m depth to the bottom. This calculation will be performed by first proving that, in regions where the sound speed varies linearly with depth, the ray paths form arcs of circles.

*To prove that if the sound speed varies linearly with depth, the rays follow arcs of circles*

To begin, Snell's law allows statement of the relation between the sound speed at a particular depth and the angle,  $\theta$ , which a ray at that depth makes locally with the horizontal. If at depth  $d_n$  the sound speed is  $c_n$  and the ray path has an angle  $\theta_n$  to the horizontal, then

$$\cos \theta_1 / c_1 = \cos \theta_2 / c_2 = \cos \theta_i / c_i \quad (7.9)$$

where the terms are defined through the scheme shown in Fig. 7.9. A sound ray is initially travelling horizontally, passing through point  $X_i$  at a depth  $d_i$  with speed  $c_i$ . It then passes through point  $X_1$  at a depth  $d_1$  with speed  $c_1$ ,

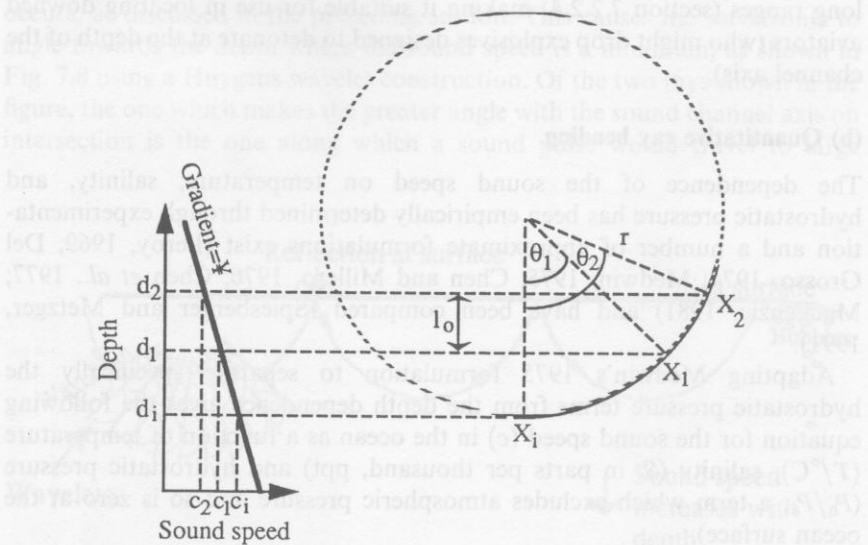


**Figure 7.9** Ray paths in a region of ocean where the sound speed increases linearly with depth.



and then passes point  $X_2$  at a depth  $d_2$  with speed  $c_2$ . The ray is an arc of a circle if it satisfies two conditions:

The first condition is that, if the ray follows a circle arc, then the circle has radius  $r$  such that the distance  $l_0$  on the figure is:

$$l_0 = r \cos \theta_1 - r \cos \theta_2 = d_1 - d_2 . \quad (7.10)$$

Since the variation is linear, with gradient  $\mathbb{Y}$ ,

$c_1 = c_i + \mathbb{Y}(d_1 - d_i)$  and  $c_2 = c_i + \mathbb{Y}(d_2 - d_i)$  which implies that

$$d_1 - d_2 = (c_1 - c_2)/\mathbb{Y} . \quad (7.11)$$

The second condition is that, if the circle arc is a ray, Snell's Law must be satisfied, i.e. from equation (7.9):

$$c_1 = c_i \cos \theta_1 \text{ and } c_2 = c_i \cos \theta_2 \text{ (since } \cos \theta_i = 1) . \quad (7.12)$$

Substituting equation (7.11) into (7.10) gives:

$$(c_1 - c_2)/r\mathbb{Y} = \cos \theta_1 - \cos \theta_2 . \quad (7.13)$$

Substituting equation (7.12) into (7.13) gives:

$$\begin{aligned} (c_1 - c_2)/r\mathbb{Y} &= c_1/c_i - c_2/c_i, \text{ i.e. } \frac{(c_1 - c_2)}{r\mathbb{Y}} = \frac{(c_1 - c_2)}{c_i} \\ \Rightarrow r &= \frac{c_i}{\mathbb{Y}} \end{aligned} \quad (7.14)$$

If both conditions are satisfied, and the ray is a circle arc. Similarly, if the sound speed decreases with depth,

$$r = -\frac{c_i}{\mathbb{Y}} \quad (7.15)$$

the negative sign in the context of the geometry of Fig. 7.9 indicating that, in such circumstances, the ray curves downwards (in agreement with the discussions of section 7.2.2.3a). In general therefore, if  $h$  is the depth below the surface, then

$$\left| \frac{dc_0}{dh} \right| = \frac{c_i}{\text{radius of curvature}} . \quad (7.16)$$

With this formulation, it is possible to use equation (7.8) to approximate for the sound speed profile by two regimes in which the sound speed varies linearly with depth. The first regime is at depths above the sound speed axis, and the second is below it.

*To evaluate the linear approximations to the sound speed profile*

The values of the sound speeds, and the sound speed gradient, for the example section of the ocean chosen can be found from equation (7.8). For  $S = 35$  parts per thousand, the sound speed varies as

$$c_0 = 1449.2 + 4.6T - 0.055T^2 + 0.0003T^3 + 1.74 \times 10^{-6}P_h \text{ m/s} \quad (7.17)$$

The temperature is given by

$$T/^{\circ}\text{C} = 10 - 10h/1000 = 10 - 0.01h \quad (\text{for } 0 \leq h/\text{m} \leq 1000) \quad (7.18)$$

$$T/^{\circ}\text{C} = 0 \quad (\text{for } 1000 \leq h/\text{m} \leq 6000) \quad (7.19)$$

and the hydrostatic pressure is related to the depth through

$$1.74 \times 10^{-6}P_h = 1.74 \times 10^{-6}\rho_0gh \approx 0.017h \quad (7.20)$$

where  $g$  is the acceleration due to gravity. Substituting equations (7.18) to (7.20) into equation (7.17) gives the sound speed as a function of depth only in the two regions above and below 1000 m depth:

$$\begin{aligned} \frac{c_0(h \leq 1000 \text{ m})}{\text{m/s}} &\approx 1449.2 + 4.6(10 - 0.01h) \\ &\quad - 0.055(10 - 0.01h)^2 + 0.0003(10 - 0.01h)^3 + 0.017h \\ &= 1490 - 0.0189h - 4.6 \times 10^{-6}h^2 - 3 \times 10^{-10}h^3 \\ &\quad (\text{for } 0 \leq h/\text{m} \leq 1000) \end{aligned} \quad (7.21)$$

$$c_0(h \geq 1000 \text{ m}) \approx 1449.2 + 0.017h \text{ m/s} \quad (\text{for } 1000 \leq h/\text{m} \leq 6000). \quad (7.22)$$

At  $h = 1000$  m, equations (7.21) and (7.22) give sound speeds of 1466.3 m/s and 1466.2 m/s respectively. While equation (7.22) predicts that below 1000 m depth the sound speed varies linearly with depth, above  $h = 1000$  m the following relation (derived from equation (7.22)) is only approximately true:

$$c_0(h \leq 1000 \text{ m}) \approx 1490 - 0.0189h \text{ m/s} \quad (\text{for } 0 \leq h/\text{m} \leq 1000) \quad (7.23)$$

giving, at  $h = 1000$  m, a speed of sound of 1471.1 m/s, in disagreement with equations (7.21) and (7.22), indicating the error in the approximation. The linear sound speed gradient assumed for the two regimes is therefore, from equations (7.22) and (7.23):

$$dc_0/dh \approx -0.0189 \text{ s}^{-1} \quad (\text{for } 0 \leq h/\text{m} \leq 1000) \quad (7.24)$$

$$dc_0/dh = +0.017 \text{ s}^{-1} \quad (\text{for } 1000 \leq h/\text{m} \leq 6000) \quad (7.25)$$

*To find the approximate path followed by a ray projected horizontally at the surface*

It is now possible to consider a ray which is projected at the surface in a horizontal direction, and estimate the greatest depth achieved by the ray, and the horizontal distance between the source and the point where the ray returns to the surface. Figure 7.10 schematically shows the ray in question,

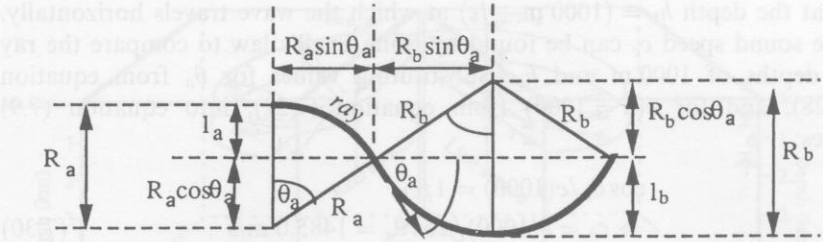


**Figure 7.10** A ray, travelling from the surface to the position of its deepest descent, and then back to the 1000 m depth, within the model ocean profile (the radii of curvature are shown much reduced for clarity).

travelling from the surface to the position of its deepest descent, and then back to the 1000 m depth.

Consider when the ray is at depths less than 1000 m. It moves in an arc of a circle of radius  $R_a$ , which can be calculated by substituting the sound speed gradient ( $= -0.0189$ ) from equation (7.24) and sound speed at the surface (the depth at which the wave travels horizontally) into, say, equation (7.15). The sound speed at the surface is found from equation (7.21) for the conditions  $h = 0$ :

$$c_0(h = 0) = 1490 - 0.0189h - 4.6 \times 10^{-6}h^2 - 3 \times 10^{-10}h^3 = 1490 \text{ m/s} . \quad (7.26)$$

Therefore from equation (7.16) the radius of curvature at depths of less than 1000 m is:

$$|R_a| = |c_0(h = 0)/(dc/dh)| = 1490/0.0189 \approx 78.836 \text{ km} . \quad (7.27)$$

After descending a depth  $l_a = 1000$  m, it has travelled through an arc angle of  $\theta_a$ , where from Fig. 7.10, the geometry indicates

$$l_a = R_a(1 - \cos \theta_a) \text{ implying}$$

$$\theta_a = \cos^{-1}(1 - l_a/R_a) = \cos^{-1}(1 - 1000/78\,836) = 9.14^\circ . \quad (7.28)$$

By the time it reaches a depth of 1000 m (for the first time) it is a distance  $x_a$  from the source, which can be evaluated by substituting values from equations (7.27) and (7.28) into geometrical consideration of Fig. 7.10:

$$x_a = R_a \sin \theta_a = 12\,517 \text{ m} . \quad (7.29)$$

Now consider the ray when it is at depths of greater than 1000 m. It travels in an arc of radius  $R_b$ , which can be calculated using knowledge of the sound speed gradient ( $= 0.017$  from equation (7.25)) and sound speed

$c_b$  at the depth  $h_b = (1000 \text{ m} + l_b)$  at which the wave travels horizontally. The sound speed  $c_c$  can be found by using Snell's law to compare the ray at depths of 1000 m and  $h_b$ . Substituting values for  $\theta_a$  from equation (7.28), and for  $c(h = 1000)$  from equation (7.22), into equation (7.9) gives:

$$\begin{aligned}\cos \theta_a / c(1000) &= 1 / c_b \\ \Rightarrow c_b &= c(1000) / \cos \theta_a = 1485.0 \text{ m/s} .\end{aligned}\quad (7.30)$$

Therefore from equation (7.16) the radius of curvature at depths of greater than 1000 m is:

$$|R_b| = |c_b / (dc/dh)| = 1484.8 / 0.017 = 87\,355 \text{ m} .\quad (7.31)$$

Knowledge of this radius allows, from geometrical consideration of Fig. 7.10, estimation of the maximum depth attained by the ray,  $h_b$ , which is given by

$$h_b = (1000 \text{ m} + l_b) = (1000 \text{ m} + R_b(1 - \cos \theta_a)) = 2108 \text{ m} .\quad (7.32)$$

Applying symmetry considerations to Fig. 7.10, the horizontal distance travelled before the ray reaches the surface is given by

$$2(R_a \sin \theta_a + R_b \sin \theta_a) = 2(12\,517 \text{ m} + 13\,868 \text{ m}) = 52.770 \text{ km} .\quad (7.33)$$

In this model ocean profile, the ray, which was projected horizontally at the surface, returns to the surface nearly 53 km later, then to repeat the motion (so long as the sound speed profile persists). (To visualize the scale, imagine a pulse, descending from the surface into the dark depths at speeds in excess of a kilometre a second. The direction followed dips at a shallow, but ever-increasing, angle to the horizontal, reaching a maximum of  $\sim 9^\circ$  at 1 km depth. It has taken the pulse about 8.5 seconds to travel the path length of  $\sim 12.6$  km thus far. The angle now begins to decrease as the pulse descends further, to depths even sperm whales cannot attain, the sound speed increasing until at a depth of  $\sim 2.1$  km the pulse is travelling horizontally. Here there is no light, little dissolved oxygen, and few fish. Since starting, the pulse has travelled a path length of  $\sim 26.5$  km, taking around 18 seconds. The pulse begins to rise now, the angle to the horizontal first increasing then decreasing until, at the surface 53 km from the start position, it is horizontal once more. The 36 s taken is very close to the time required were a horizontal direct path to exist, illustrating how, because of the shallow angles involved, when viewed on the large scale the path is not dissimilar to the straight line. This will be re-examined in Fig. 7.11). Such distances (53 km) are characteristic of 'convergence zones'. These zones will be discussed in the companion volume to this book, as will the related phenomena of 'shadow zones' and 'caustics'. These are regions devoid of rays, and regions of partial focusing respectively.

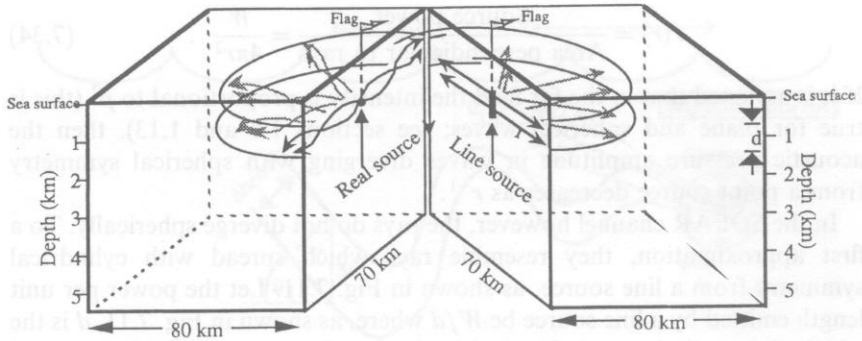


**Figure 7.11** Schematic illustration showing how, to first-order approximation, ray propagation in the SOFAR channel may be likened to cylindrical spreading. A section of ocean of over 5 km depth, having a sound speed minimum at 1 km depth, is cut into two halves, which are folded away from one another for clarity. A sound speed profile similar to that shown in Fig. 7.5 is assumed. The horizontal distance scale is much less than the vertical, such that the half-spaces are each  $80 \text{ km} \times 70 \text{ km}$  in the horizontal plane (distances estimated from equation 7.33). The vertical plane of the cut passes through the acoustic source, which is placed at 1 km depth (and marked at the surface by a flagged buoy). Two of the ray paths from the buoy are illustrated, propagating into the half-space of a disc which roughly indicates the vertical extent of the SOFAR channel. If the sound speed profile is uniform throughout the section of ocean illustrated, the ray propagation will be identical in all horizontal radial directions out from the source (i.e. there is rotational symmetry about the vertical axis which passes through the source). However the rays in only five directions per half-space are shown for clarity. In the right half-space the ray paths for cylindrical spreading from a line source are shown, indicating the degree of similarity with the oceanic rays paths, which are sketched in the left-hand half. The similarity, when viewed on the scale of tens of kilometres, between the curved ray path and the straight-line horizontal path, was discussed in the paragraph below equation (7.33).

#### 7.2.2.4 Long-range propagation in the SOFAR channel

##### (a) Geometrical losses

Having indicated the nature of ray propagation in acoustic channels, in this section the reduction in signal-to-noise amplitude due to geometrical spreading will be discussed. Absorptive losses which convert acoustic energy into heat will not be included until section 7.2.2.4(b).

In section 1.13, it was shown that when acoustic waves diverge with spherical symmetry from a point source, the intensity  $I(r)$  decreases with distance from the source  $r$  as an inverse-square law, e.g. for a source of constant power  $W$ :



$$I(r) = \frac{\text{Source power}}{\text{Area perpendicular to rays}} = \frac{W}{4\pi r^2} \quad (7.34)$$

If it is assumed that in the far field the intensity is proportional to  $p^2$  (this is true for plane and spherical waves; see sections 1.8 and 1.13), then the acoustic pressure amplitude in waves diverging with spherical symmetry from a point source decreases as  $r^{-1}$ .

In the SOFAR channel however, the rays do not diverge spherically. To a first approximation, they resemble rays which spread with cylindrical symmetry from a line source, as shown in Fig. 7.11. Let the power per unit length emitted by a line source be  $W/d$  where, as shown in Fig. 7.11,  $d$  is the width of the cylinder, and also the length of the line source (which emits rays only perpendicular to its length). The intensity  $I(r)$  at radius  $r$  (measured on a radius perpendicular to the line source, as shown in Fig. 7.11) is therefore:

$$I(r) = \frac{\text{Source power}}{\text{Area perpendicular to rays}} = \frac{W}{2\pi r d} \quad (7.35)$$

Therefore, if there are no absorptive losses, and if the approximation is made that a cylindrically diverging system can model the SOFAR channel, then geometrical spreading causes the acoustic intensity to decrease with distance as  $1/r$ . If it is further assumed that, within the limits of the approximation, intensity is proportional to  $p^2$  (see above), the model predicts that acoustic pressure amplitude will decrease with distance as  $1/\sqrt{r}$ . The geometrical losses are therefore less than those expected for spherical divergence.

It is not necessary to limit geometrical considerations to making the approximation that the rays follow radial paths perpendicular to a given central axis. Urick (1983) compares the intensities close to, and distant from, the source. From their ratio the concept of 'transmission loss' will now be introduced. Consider two rays which leave the source, where the sound speed is  $c_1$ , at angles  $\theta_1 + \Delta\theta/2$  and  $\theta_1 - \Delta\theta/2$ . The power radiated by the source into  $\Delta\theta$  is  $\Delta W$ . The rays, travelling with rotational symmetry about the vertical axis which passes through the centre of the source, subtend an area  $\Delta A_1$  at a radius  $r_1$  from source, such that the power flux through  $\Delta A_1$  (the shaded area on the sphere of radius  $r_1$  in Fig. 7.12) is:

$$I(r_1) = \frac{\Delta W}{\Delta A_1} = \frac{\Delta W}{2\pi r_1 \cos \theta_1 (r_1 \Delta\theta)} \quad (7.36)$$

No matter how complicated the ray paths, the two rays travel to a point  $X$  where the sound speed is  $c_2$ , a horizontal distance  $r$  from the source (see Figs 7.11 and 7.12), where they both subtend an angle of approximately  $\theta_2$  to the horizontal, and have a vertical separation  $\Delta h$ . Maintaining the assumption of no absorptive losses, and assuming that there has been no leaking out of energy contained between the two rays, then between them the rays still

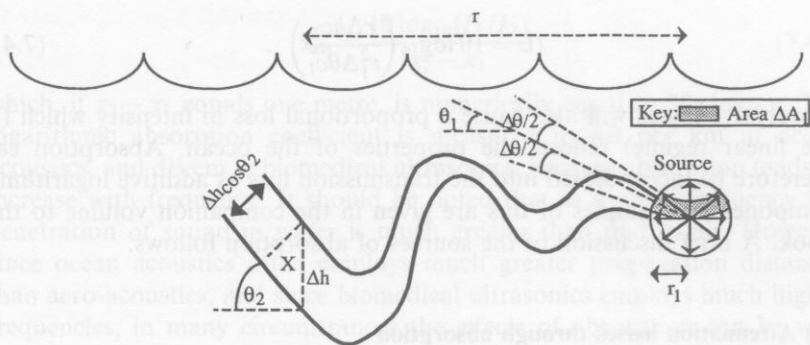


**Figure 7.12** Schematic of two rays used for calculation of geometric spreading losses (dimensions and angles not to scale). After Urick (1983).

carry power  $\Delta W$ . Therefore the intensity at  $X$  corresponds to the distribution of this power over the area element  $\Delta A_2$  between the rays and perpendicular to them. Recalling the rotational axis of symmetry, the width of this area strip corresponds to the distance between the two rays at  $X$ , measured normal to them, which from Fig. 7.12 is  $\Delta h \cos \theta_2$ . Because of the cylindrical symmetry, the area  $\Delta A_2$  is

$$\Delta A_2 = 2\pi r \Delta h \cos \theta_2 \quad . \quad (7.37)$$

Therefore the intensity at  $X$  under these conditions is

$$I(r_2) = \frac{\Delta W}{\Delta A_2} = \frac{\Delta W}{2\pi r \Delta h \cos \theta_2} \quad (7.38)$$

Several parameters, which may be unknown, are eliminated when the ratio of  $I_1/I_2$  is taken. Indeed, this quantity relates not to the source, but to the characteristics of the propagation paths and therefore to the ocean environment. It is therefore convenient to discuss the proportion by which intensity is reduced through this ratio, in terms of the Transmission Loss,  $TL$ , which is here given by

$$TL = 10 \log_{10} \left( \frac{I_1}{I_2} \right) = 10 \log_{10} \left( \frac{\Delta A_2}{\Delta A_1} \right) \quad (7.39)$$

giving

$$TL = 10 \log_{10} \left( \frac{2\pi r \Delta h \cos \theta_2}{2\pi r_1^2 \Delta \theta \cos \theta_1} \right). \quad (7.40)$$

Through application of Snell's Law (equation (7.9)), the angles which the rays subtend to the horizontal can be eliminated, allowing the transmission loss to be expressed in terms of the angular ray separation, sound speeds, and accessible distances:

$$TL = 10 \log_{10} \left( \frac{r \Delta h c_2}{r_1^2 \Delta \theta c_1} \right) . \quad (7.41)$$

Absorptive losses will also cause a proportional loss in intensity which (in the linear regime) reflects the properties of the ocean. Absorption can therefore be incorporated into the transmission loss as additive logarithmic components. Examples of this are given in the companion volume to this book. A brief discussion of the sources of absorption follows.

### (b) Attenuation losses through absorption

In the previous section, the contribution to the decrease in signal amplitude which results from the geometrical spreading was discussed. In that scenario, the acoustic energy was conserved during propagation. However in practice this will not be the case, and during propagation the acoustic energy will be converted, ultimately, to heat, through a range of mechanisms. In this section, these mechanisms will be discussed. This phenomenon, as will be seen in section 7.4.3.1, is also an important consideration in the use of medical ultrasound, because of the loss in signal amplitude and also for bioeffect considerations.

From Chapter 1, a plane progressive pressure wave of single frequency, travelling in the  $x$ -direction in an absorbing medium, can be expressed as

$$p = p_0 e^{j(\omega t - kx)} e^{-\alpha x} . \quad (7.42)$$

Given that in this wave intensity is proportional to the square of the pressure, then it will decay as  $e^{-2\alpha x}$ . The units of the attenuation coefficient,  $\alpha$ , which is defined through equation (7.42) and therefore has dimensions of  $[\text{length}]^{-1}$ , are termed nepers per metre (Np/m). The phenomenon may also be quantified by the *logarithmic absorption coefficient*,  $\alpha_{\text{ab}}$ , which can be illustrated using plane waves (in which the geometric losses are zero), through consideration of the intensity  $I(x)$  as a function of  $x$ , the distance from source. Since, as shown earlier, the intensity is proportional to  $p^2$ , equation (7.42) allows expression of the proportional intensity change during propagation as:

$$\frac{dI}{I} = -2\alpha dx \quad (7.43)$$

integration of which gives

$$I_2 = I_1 \exp(-2\alpha(x_2 - x_1)) . \quad (7.44)$$

The logarithmic absorption coefficient,  $\alpha_{\text{ab}}$ , relates to the intensity reduction over a given distance (between, say, ranges  $x_1$  and  $x_2$ , where the intensities are  $I_1$  and  $I_2$  respectively):

$$\alpha_{ab} = \frac{10 \log_{10}(I_1/I_2)}{x_2 - x_1} \quad (7.45)$$

which, if  $x_2 - x_1$  equals one metre, is numerically equal to  $20\alpha \log_{10} e$ . The logarithmic absorption coefficient is measured in dB per km in ocean acoustics, and dB/cm in biomedical ultrasonics, because absorption tends to increase with frequency. It should be noted that at a given frequency the penetration of sound in water is much greater than that in air. However since ocean acoustics often employs much greater propagation distances than aero-acoustics, and since biomedical ultrasonics employs much higher frequencies, in many circumstances the effects of absorption can be very significant in applications of underwater acoustics. Values of  $\alpha$ , the amplitude attenuation constant, are given for various materials in Table 7.1 for biomedically relevant frequency of 1 MHz. (*Derating* is required when using test results obtained with medical ultrasound fields in water to determine the appropriate field properties (e.g. peak negative pressure) that would be attained *in vivo* in body fluids, to account for attenuation and nonlinear propagation.) Values pertinent to the ocean will be indicated after a consideration of the relevant mechanisms.

The acoustic absorption of seawater is much higher than that of pure water (30 times greater in the frequency range 5–50 kHz). The causes of this are mechanisms associated with shear and volume viscosity, and, below 100 kHz, a dominant loss mechanism is the ionic relaxation of magnesium sulphate. The cumulative contributions of these effects to the *logarithmic absorption coefficient*,  $\alpha_{ab}$ , are shown as a function of frequency in Fig. 7.13. Below 5 kHz, the attenuation is higher than would be expected through the ionic relaxation of magnesium sulphate alone, and the extra mechanisms proposed include: high amplitude shock wave effects; diffraction and scattering from the SOFAR channel (not strictly a process by which acoustic

**Table 7.1** Specific acoustic impedance and attenuation

	Density (kg/m <sup>3</sup> )	Speed of sound in the bulk (m/s)	Specific acoustic impedance (kg/m <sup>2</sup> s)	Amplitude attenuation coefficient (Neper/m) at 1 MHz
Air at STP	1.2	330	400	138
Water	1000	1480	$1.5 \times 10^6$	0.0253
Castor oil	950	1500	$1.4 \times 10^6$	10.9
PMMA (polymethyl-methacrylate)	1190	2680	$3.2 \times 10^6$	23.0
Aluminium	2700	6400	$1.7 \times 10^7$	0.0207
Brass	8500	4490	$3.8 \times 10^7$	0.230

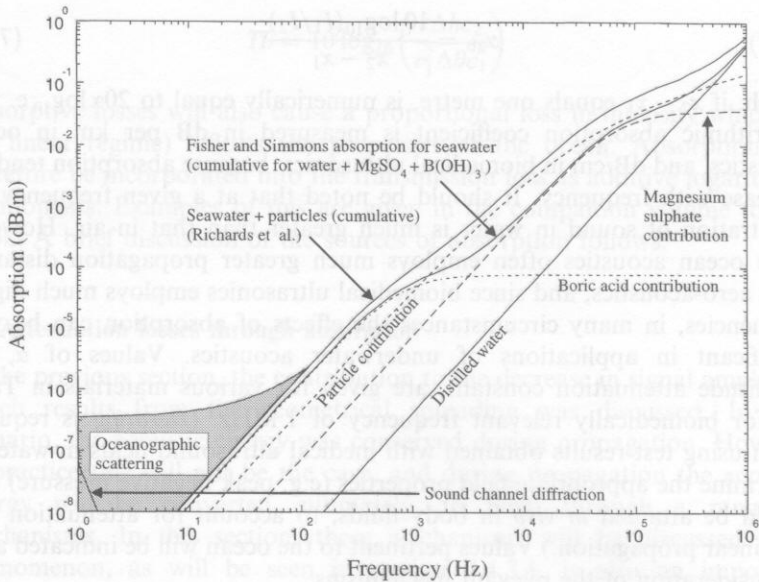


**Figure 7.13** The frequency dependence of contributions to the logarithmic absorption coefficient by: pure water; the contribution from magnesium sulphate ionic relaxation; the contribution from boron–borate relaxation; the Fisher and Simmons calculation of the cumulative effects of absorption in seawater, including the contributions from magnesium sulphate ionic relaxation and from boron–borate relaxation; and the contributions from oceanographic scattering and, at low frequency, diffraction from the SOFAR channel. Seawater contributions were computed using the Fisher and Simmons methods, employing a model for seawater of Lyman and Fleming (1940) for  $T = 4^\circ\text{C}$ ,  $S = 35$  ppt, and an ambient pressure of 1 bar. The contribution of a particulate suspension to the absorption was computed using the model of Richards *et al.* (1996), for a concentration of  $0.2\text{ kg/m}^3$  of spherical quartz particles of  $3\text{ }\mu\text{m}$  radius; both this contribution, and the effect on the cumulative absorption, when this is added to the Fisher and Simmons seawater model, are shown. (T.G. Leighton, R.C. Evans).

energy is converted into heat, but included here since the energy in such ray paths does not fit the cylindrical spreading model of the previous section); eddy viscosity; and the influence of solid particulates (Richards *et al.*, 1996). Current theory attributes a contribution to the excess absorption at these lower frequencies to boron–borate relaxation, a process which is dependent on the pH of the ocean. Ionic processes involving magnesium carbonate contribute to a lesser extent. Below about 100 Hz scattering by large inhomogeneities in the SOFAR sound channel contribute to the absorption. These processes are detailed by Urick (1983).



### (c) Ocean acoustic thermometry

Because of the geometrical effects outlined in section 7.2.2.4(a), acoustic signals will propagate to long range in the SOFAR channel. This facility has been exploited over the years in many ways, which are detailed in the references given at the start of the chapter, and as such will not be considered here. However in recent years a new technique has arisen which exploits this effect, Acoustic Thermometry of Ocean Climate (ATOC), and this will be discussed briefly. For further details see, for example, Munk and Baggeroer (1994), which is an introductory article to a further seventeen papers in the same volume.

Consider Fig. 7.8. As discussed in section 7.2.2.3(a), of the two rays shown in the figure, the one which makes the greater angle with the sound channel axis on intersection is the one along which a sound pulse would travel to distance with the least propagation time. This is a general trend, which occurs since the longer path travels through regions of greater sound speed. Now consider an experiment in which a single impulse is generated from an acoustic source placed on the axis of the SOFAR channel. The receiver will detect a series of impulses corresponding to the different travel times along the various ray paths. If a propagation model using an assumed temperature profile predicts arrivals at a distant receiver hydrophone of a form sketched in Fig. 7.14(a), but instead the experiment records arrivals of

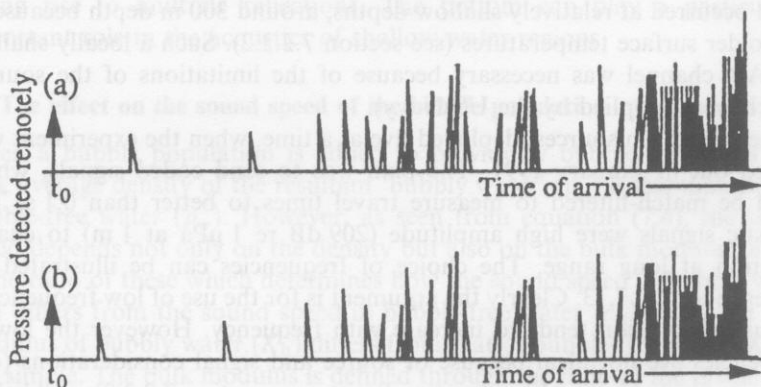


**Figure 7.14** A schematic illustration of arrival times of acoustic pulses detected remotely when a source delivers a single impulse into the SOFAR channel. The earliest arrivals (to the left of the trace) correspond to ray paths which travel far away from the sound speed axis. To the right, the closely-spaced arrivals are from ray paths which keep nearer to the axis. In this imagined experiment, (a) shows the predicted time-history from an assumed sound speed profile, and (b) illustrates a time-history the detection of which would indicate that off-axis temperatures are greater than those assumed in the model profile employed in (a).



the form sketched in Fig. 7.14(b), the indications are that the on-axis temperatures assumed in the model are correct, but that off-axis the sea is warmer (since earlier arrivals, as discussed above, correspond to the rays that diverge further off-axis).

This is a very simple example but illustrates the principle which, it was proposed, might be exploited to monitor global warming. Global warming measurements are often complicated by spatial variation. Since the speed of sound is temperature dependent in water, the spatially averaged temperature can be inferred using propagation over large distance, up to thousands of kilometres.

The sound speed increases by 4.6 m/s per degree centigrade. It is estimated that, at around 1 km depth in the ocean, the average temperature might be expected to increase by 0.004 K per year (an exponential extrapolation of a 20 mK/year increase at the ocean surface, which would predict a 1.8 mm/year sea level rise resulting from thermal expansion alone – Baggeroer and Munk (1992)). Therefore over an 18 000 km travel path (half way around the world), over a year the travel times would be expected to decrease by around 0.15 s, which is clearly measurable. While explosive sources had generated sound detectable at global ranges, to detect such changes a well-characterized, non-explosive source was required.

The source site was identified at Heard Island in the Southern Indian Ocean – from here both the Atlantic and Pacific Basins could be insonified. Being at high latitudes, it was in a region where the minimum in the sound speed occurred at relatively shallow depths, around 300 m depth because of the colder surface temperatures (see section 7.2.2.2). Such a locally shallow SOFAR channel was necessary because of the limitations of the sources (which were supplied by the US Navy).

There were ten sources, deployed five at a time, when the experiment was carried out in January 1991. The plan was to send coded signals, which could be match-filtered to measure travel times to better than 0.1 s. The acoustic signals were high amplitude (209 dB re 1  $\mu$ Pa at 1 m) to enable detection at long range. The choice of frequencies can be illustrated by reference to Fig. 7.13. Clearly the argument is for the use of low frequencies, because absorption tends to increase with frequency. However the lowest frequencies are not ideal because of source and signal considerations (e.g. the noise from shipping becomes significant – see section 7.2.3.2), and below 10 Hz there is no great benefit in reducing frequency because oceanographic scattering generates losses which do not decrease with frequency significantly (see Fig. 7.13).

Frequency limitations of the propagation models to be used are also a consideration. For the Heard Island tests, a carrier frequency of 57 Hz was chosen to avoid the electricity mains frequencies of 50 Hz (e.g. UK) and 60 Hz (USA). Subsequent experiments included, in April 1994, propagation of 19.6 Hz signals over 2600 km paths in ice-covered water under the Arctic

(Mikhalevsky and Baggeroer, 1995), where the sound speed profile is usually upwardly refracting from the bottom to the surface because the surface temperatures are colder than those at depth.

### 7.2.2.5 Sea surfaces and the sound speed

The parameters which control the sound speed, and the consequences and pertinent phenomenon in the deep ocean (e.g. long-range propagation in the SOFAR channel and the role in this of attenuation) have been discussed in section 7.2.2. The sound speed in the sea boundaries, the bottom and the atmosphere/ocean interface will now be introduced.

#### (a) The sea bottom

The acoustics of the sea bottoms are detailed in the references cited at the outset of this chapter and will not be discussed in depth here. Suffice to say that bottoms may have a range of compositions from hard rock to sediments; that though the density of the bottom is usually greater than that of water, the sound speed can be either greater than or less than water (mud bottoms alone might have a sound speed greater than or less than water); that waves other than compressional may propagate (shear waves, surface waves etc.); that the surface may have varying degrees of roughness; and that a given bottom may contain inhomogeneities and even be stratified, giving rise to multiple reflections. The bottom can play a particularly important role in the acoustics of shallow water regions.

#### (b) The effect on the sound speed of the bubble population

When a bubble population is added to previously bubble-free water, the bulk average density of the resultant 'bubbly water' ( $\rho_b$ ) is less than that of bubble-free water ( $\rho_w$ ). However, as seen from equation (7.4), the sound speed depends not only on the density but also on the bulk modulus, and it is the ratio of these which determines how the sound speed in bubbly water ( $c_b$ ) differs from the sound speed in bubble-free water ( $c_w$ ). How the bulk modulus of bubbly water ( $K_b$ ) differs from that of bubble-free water ( $K_w$ ) is not simple. The bulk modulus is defined through the ratio of the proportion change in volume ( $dV/V$ ) to the change in total fluid pressure ( $dP$ ) which brings about the volume change:

$$K = -V \frac{dP}{dV} . \quad (7.46)$$

The negative sign is employed because, in the quasi-static case, an increase in pressure leads to a reduction in volume, so that  $dP$  and  $dV$  normally have opposite sign, making  $K$  a positive quantity. Question 7.5.2(b) illustrates from the quasi-static case a simple calculation showing how the sound speed

might be reduced by the introduction of bubbles. It is important to realize, however, that the effect on the sound speed of pulsating bubbles is a dynamic one. Here the relative phases of the oscillating pressure in the liquid and the bubble volume change are not so simply related as in the quasi-static case. This is because the bubble acts as an oscillator with a resonance frequency  $f_o$  which is related approximately inversely to its equilibrium radius  $R_o$ . For air bubbles in water under one atmosphere static pressure this relationship is given by

$$R_o f_o \approx 3 \text{ Hz.m} \quad (7.47)$$

Bubbles much larger than the radius  $R_r$  which would be resonant with a sound field of frequency  $f$  pulsate in antiphase to those having radii much smaller than  $R_r$ : the phase relationship is illustrated schematically in Fig. 7.15. If the bubble is much smaller than the resonant size ( $R_o \ll R_r$ ), or

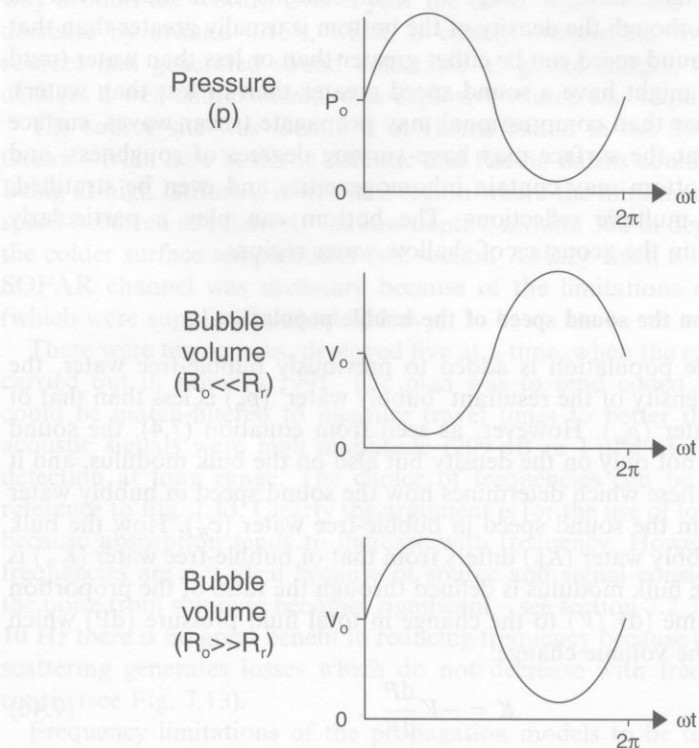


**Figure 7.15** Schematic representation of the phase relationships between a driving acoustic field and the pulsations of bubbles which are much greater than, or much less than, resonance size.

if the frequency of the acoustic field is much less than the bubble resonance ( $f \ll f_o$ ), then the bubble is compressed during the positive half-cycle of the acoustic field, and  $dP/dV$  is negative. The conditions are quasi-static as in Question 7.6.2 (b). The volume changes undertaken by the bubble serve to reduce the bulk modulus to below that of bubble-free water, and the sound speed is reduced. If, however, the bubble is much larger than the resonant size ( $R_o \gg R_r$ ), or if the frequency of the acoustic field is much greater than the bubble resonance ( $f \gg f_o$ ), then the bubble is expanded during the positive half-cycle of the acoustic field, and  $dP/dV$  is positive. The bubble presence actually contributes an expansive element under compressive forces, and the bulk modulus of bubbly water is greater than that of bubble-free water, so that the bubble presence tends to increase the sound speed. The effect is greater the larger the amplitude of bubble volume oscillation, which will be highest at resonance.

Simple expressions can be stated for the sound speed when the acoustic frequency and number density of bubbles take extreme values (Leighton, 1994, §3.8.2(b)). In the limit of low acoustic frequencies and high number densities of bubbles of the same size, the sound speed in a bubble cloud is approximately

$$c_b \approx \sqrt{\frac{\gamma p_o}{\rho_w \{VF\}}} \quad (7.48)$$

if the gas in the bubbles behaves adiabatically. In the isothermal limit,

$$c_b \approx \sqrt{\frac{p_o}{\rho_w \{VF\}}} \quad (7.49)$$

where  $\{VF\}$  is the 'void fraction' (strictly the gas-volume fraction). For the example of Question 7.6.2 (b) (where the void fraction of  $10^{-4}$  is relatively high, and which, being quasi-static, is valid for low insonation frequencies), equations (7.48) and (7.49) predict sound speeds of 1183 m/s and 1000 m/s respectively. In the opposite limit of a low number density ( $n_b$ ), the sound speed in cloud of bubbles, all of radius  $R_o$ , is

$$c_b = c_w \left\{ 1 - \left( \frac{2\pi R_o n_b c_w^2}{\omega^2} \right) \left( \frac{(\omega_o/\omega)^2 - 1}{\left\{ (\omega_o/\omega)^2 - 1 \right\}^2 + d^2} \right) \right\} \quad (7.50)$$

where  $d$  gives the bubble pulsation damping

This equation is plotted in Fig. 7.16 for  $R_o = 0.1$  mm and varying  $n_b$ . At low insonation frequencies ( $\omega \ll \omega_o$ ), equation (7.50) reduces to

$$c_b = c_w \left\{ 1 - \left( \frac{2\pi R_o n_b c_w^2}{\omega_o^2} \right) \right\} \quad (7.51)$$

which reduces to

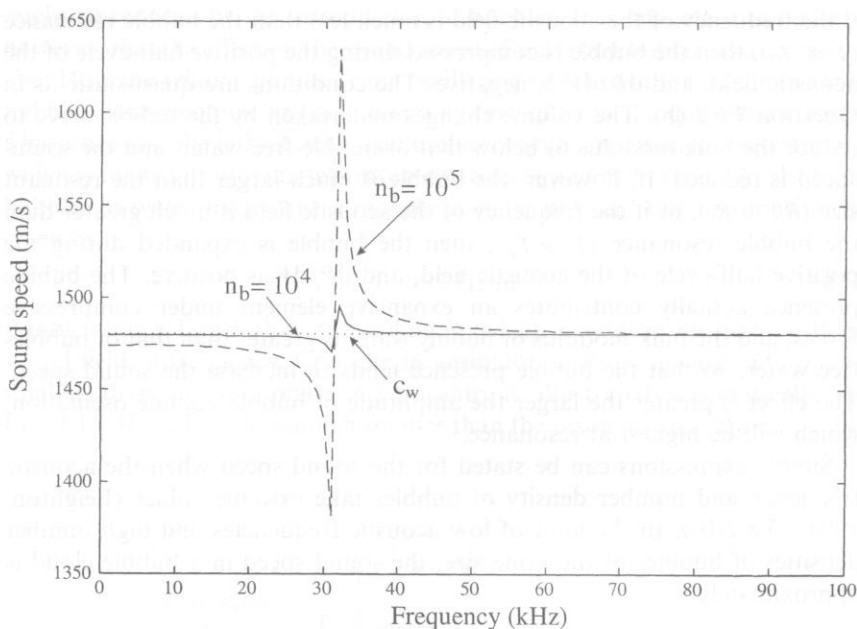


**Figure 7.16** Plot of the sound speed as a function of the acoustic frequency for a population of bubbles, all having  $R_0 = 0.1$  mm, with the number densities shown ( $n_b/\text{m}^{-3}$ ). The sound speed for bubble-free water,  $c_w$ , is shown.

$$c_b \approx c_w \left\{ 1 - \frac{1}{2} \{VF\} \frac{\rho c_w^2}{\kappa p_o} \right\}. \quad (7.52)$$

Usually there is a distribution of bubble sizes within the cloud, such that  $n_b^{gr}(z, R_0) dR_0$  is the number of bubbles per unit volume at depth  $z$  having radii between  $R_0$  and  $R_0 + dR_0$ , and the speed of sound is a function of both the depth and the acoustic frequency:

$$c_b(z, \omega) = c_w \left\{ 1 - (2\pi c_w^2) \int_{R_0=0}^{\infty} \frac{R_0}{\omega^2} \left( \frac{(\omega_o/\omega)^2 - 1}{\{(\omega_o/\omega)^2 - 1\}^2 + d^2} \right) n_b^{gr}(z, R_0) dR_0 \right\}. \quad (7.53)$$

### (c) The oceanic bubble population

In section 7.2.2.2, the vertical variation in sound speed was introduced, though note was made that variations of sound speed in the horizontal plane occur as well because of changes in the properties of the seawater. Having discussed and quantified the role of bubbles in determining the sound speed,

the section will close with a description of how variations in the bubble population, in both the horizontal and vertical planes, can arise. Though bubbles can be introduced into the ocean through other routes (e.g. volcanic or biological action, methane seeps, etc.), the majority of bubble entrainment occurs at the atmosphere/ocean interface through wave action. While details of the breaking and evolution of bubble population under breaking waves are not known, it is possible to gain a picture from the available evidence. Much of this comes in the form of sonar scatter from subsurface bubble clouds. Strong scatter is seen both by resonant bubbles (whose high-amplitude pulsations couple well with the sound field), and with larger bubbles (which, although they do not pulsate to a significant extent, simply represent large 'inert' scatterers because of their physical size). This effect can be seen in Fig. 7.17, where the acoustic scattering cross-section (the ratio of the power scattered spherically by a bubble to the intensity of the incident plane acoustic wave which is scattered) shows a local maximum at the resonance, but increases with the bubble cross-sectional area for the larger gas bodies.

Using such scatter, it is possible to obtain an idea of the relevant processes. Figure 7.18 shows a representation of many surface and subsurface features, relevant to a windspeed of about 10 m/s, developed by Monahan and Lu (1990). It includes the stages of development of a bubble plume, illustrating the accompanying surface features. The near-surface continuous-layer of bubbles, which occurs for windspeeds in excess of 7 m/s, is not shown.

The general pattern described by Monahan and Lu is as follows. Breaking waves form surface and subsurface features, which dissipate in time to

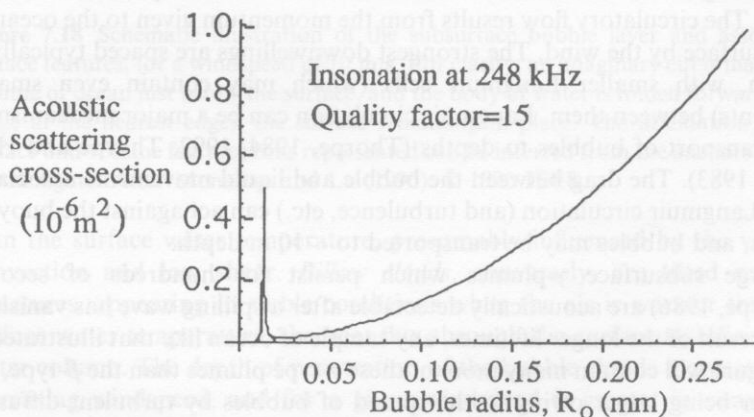


**Figure 7.17** The acoustic scattering cross-section from a single bubble as a function of the radius of that bubble, for a fixed insonation frequency of 248 kHz (with a quality factor  $Q = 15$  assumed). (after Leighton (1994), by permission of the publishers, Academic Press, London.)



eventually form a background bubble population; however the latter may itself have ordered structure imposed by large-scale circulations. Surface feature A is a spilling wave crest or active whitecap, the surface accompaniment to the subsurface concentrated bubble plume (type  $\alpha$ ). Type-A features are transient events, only persisting for longer than 1 s if they are regenerated by the parent spilling wave. Otherwise they immediately decay into the mature whitecap, or hazy foam patch, on the surface (type B features in Fig. 7.18), and a type  $\beta$  plume extending to the order of a metre below. The void fraction (i.e. % volume of bubbly water which is air as opposed to water) in type-A can be as high as 30% at the crest of the spilling wave, and from 0.01–0.02% up to 0.1–0.2% in type- $\beta$ . The void fraction decreases with depth in both (Longuet-Higgins and Turner, 1974). The B and  $\beta$  features coexist for several seconds, dissipating together. After a  $\beta$ -plume is dissipated, no subsurface features exist unless it is as the underside of stabilized foam, aggregating and persisting as a result of the surface convergence of the Langmuir circulation currents.

The concept of Langmuir circulation arose from a report in 1923 of lines of floating weed observed by Langmuir as he crossed the Atlantic, and from subsequent measurements of wind-induced surface effects in Lake George (Langmuir, 1938). That this circulation can affect the distribution and motion of surface particles is evidenced by the accumulation of foam in windrows. These are demarcated by bands of buoyant material (such as foam and weed), aligned with the wind, which occur at the line of convergence of opposing flows in Langmuir circulation. Surface active agents and oils accumulate at the line of convergence and lower the surface tension, so stabilizing the foams. Such windrows can be seen after protracted steady wind. The circulatory flow results from the momentum given to the ocean or lake surface by the wind. The strongest downwellings are spaced typically at 100 m, with smaller Langmuir cells (which may contain even smaller elements) between them. Langmuir circulation can be a major mechanism in the transport of bubbles to depths (Thorpe, 1984, 1992; Thorpe and Hall, 1980, 1983). The drag between the bubble and liquid movements associated with Langmuir circulation (and turbulence, etc.) can act against the buoyant forces, and bubbles may be transported to  $\sim 10$  m depth.

Large subsurface  $\gamma$ -plumes which persist for hundreds of seconds (Thorpe, 1986) are acoustically detectable after a spilling wave has vanished. As a result of the longer lifetimes, any sample of ocean like that illustrated in the figure will contain many more of these  $\gamma$ -type plumes than the  $\beta$ -type, the former being larger owing to the spread of bubbles by turbulent diffusion (Monahan and Lu, 1990). Thorpe (1982) used an echo sounder, located at a depth of 30 m and inverted so that it was upward-pointing, for below-surface observation of these clouds of small bubbles. The bubbles collected in two types of cloud distinguishable on sonograph records. *Columnar clouds* form during unstable or convective conditions when the air is cooler

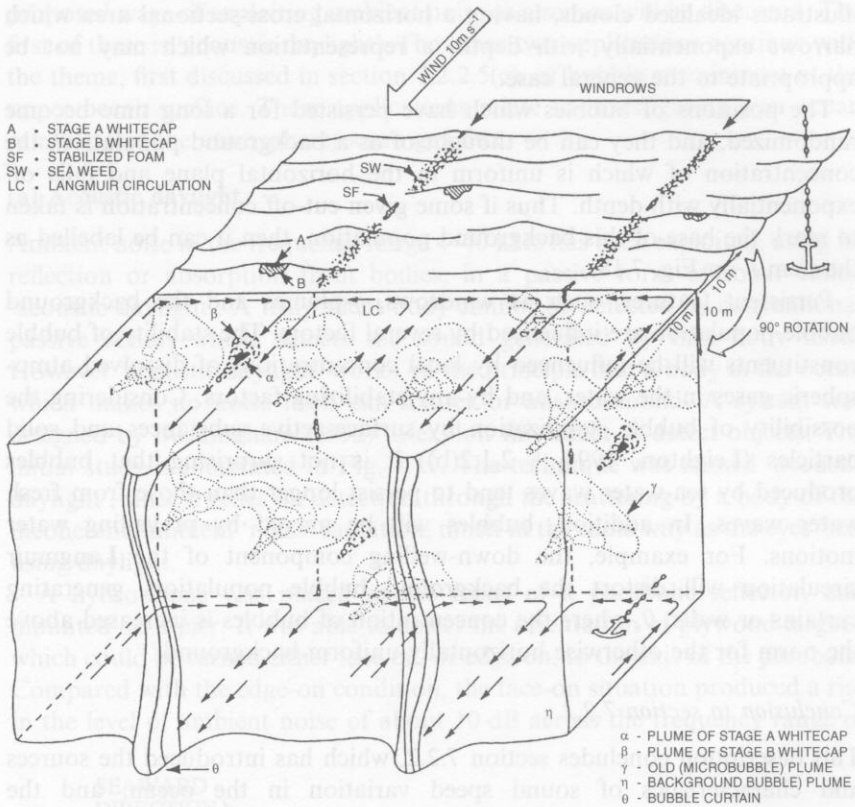


**Figure 7.18** Schematic illustration of the subsurface bubble layer and associated surface features, for a windspeed of 10 m/s. For clarity, an imaginary cut is made in a volume of ocean just below the surface, and the body of water is folded forwards (the hinge at the nearest edge), the surface remaining in place. The orientation of the surface and volume features thus represented can be inferred from the anchors drawn on the figure. After Monahan and Lu (1990). © 1990 IEEE.

than the surface water temperature, presumably influenced by the vertical convection and low shear. *Billow clouds*, conversely, are tilted roll-like structures, appearing in stable conditions when the air is warmer than the surface water temperature, the heat flux through the surface stabilizing the water column. The depth of penetration of the bubble clouds increases with increasing windspeed, and for a given windspeed is greater in convective than in stable conditions. Since small bubbles have dissolved and large ones have been removed by buoyancy, the range of bubble radii present in  $\gamma$ -plumes is narrower than those in  $\alpha$  or  $\beta$  plumes. Estimates of the void fraction suggest values of  $10^{-4}\%$  to  $10^{-5}\%$ . The concentration decreases with depth. The  $\gamma$ -plumes can be billowy or columnar, though Fig. 7.18

illustrates idealised clouds, having a horizontal cross-sectional area which narrows exponentially with depth, a representation which may not be appropriate to the general case.

The positions of bubbles which have persisted for a long time become randomized, and they can be thought of as a background population, the concentration of which is uniform in the horizontal plane and falls off exponentially with depth. Thus if some given cut-off concentration is taken to mark the base of this background population, then it can be labelled as the item  $\eta$  on Fig. 7.18.

Persistent features, such as windrows,  $\gamma$ -plumes and the background bubble population are influenced by several factors. The stability of bubble constituents will be influenced by local concentrations of dissolved atmospheric gases in the water, and by any stabilizing factors. Considering the possibility of bubble stabilization by surface-active substances and solid particles (Leighton, 1994, § 2.1.2(b)) it is not surprising that bubbles produced by sea-water waves tend to persist longer than those from fresh water waves. In addition, bubbles will be moved by prevailing water motions. For example, the down-welling component of the Langmuir circulation will distort the background bubble population, generating curtains or walls,  $\theta$ , where the concentration of bubbles is increased above the norm for the otherwise horizontally-uniform background.

### *Conclusion to section 7.2.2*

This description concludes section 7.2.2, which has introduced the sources and characteristics of sound speed variation in the ocean, and the consequences for propagation. Attention was paid to the ability to detect signals at long range because of resulting effect on geometrical spreading. This spreading, along with absorption, influenced the amplitude of the signal detected remotely. However the detectability of a signal does not depend simply on the signal amplitude. It also depends on the level of noise, the sources of which are the topic of the next section.

## **7.2.3 Sources and applications of ambient noise**

### *7.2.3.1 Applications of ambient noise*

As described at the end of the previous section, for most of the history of underwater acoustics the significance of ambient noise has been seen largely in that it generates a masking background which hinders communications and sensing. This is important, and as such a great deal of work has been undertaken in characterizing ambient noise, which is fully described in the references given at the opening of this chapter. In this section, therefore, the range of sources of ambient noise will be briefly summarized, but details will be given only on illustrative developments from the last ten years. Three

proposed ways of exploiting ambient noise as a sensor will be discussed. The first of these is 'acoustic daylight'. The other two applications continue with the theme, first discussed in section 7.2.2.5(c), of bubble entrainment at the upper ocean surface. These applications relate to investigating over-ocean rainfall, and the atmosphere/ocean gas flux.

### (a) Acoustic daylight

Ambient noise in the frequency range 4–40 kHz has been exploited, using its reflection or absorption from bodies, in a passive form of sonar called 'acoustic daylight'. A truly silent body cannot be detected by conventional passive sonar, which detects the sound generated by that body itself. However 'acoustic daylight' works on the principle that a body in the ocean which makes no noise itself can scatter or absorb sound. A system was designed by Buckingham (1992) to exploit this effect to detect objects. The initial study is illustrated in Fig. 7.19. The technique was named 'acoustic daylight', since it relies on detection through the scattering by a body of the incoherent, ambient 'noise' radiation, much in the same way as the eyes 'see' using daylight.

A hydrophone was placed at the focus of a parabolic reflector, and mounted on a pier. It was able to detect the orientation of plywood targets, which could be turned either face on, or edge on, to the axis of the parabola. Compared with the edge-on condition, the face-on situation produced a rise in the level of ambient noise of about 10 dB across the frequency range of

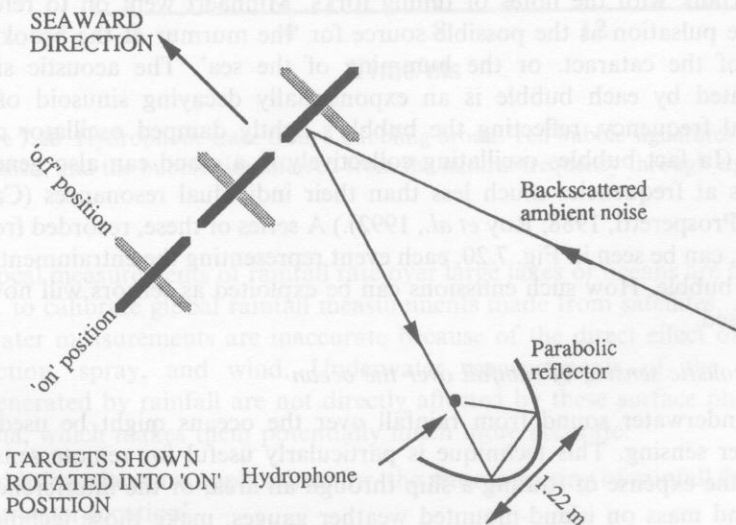


**Figure 7.19** Schematic of the apparatus used in the first acoustic daylight experiment.

4–40 kHz. The detection beam was looking out to sea, so clearly the plywood was detected through backscatter of sound produced near-shore. Later versions used an array at the focus of the parabolic reflector, instead of a single hydrophone, to generate a multi-pixel image and, by forming images from the ambient noise in different frequency bands, could generate images from both back-scatter and occlusion of the emissions from different sources of ambient noise (e.g. motor boats, shellfish etc.) (Buckingham and Epifanio, 1996). The process has also been used to form images from the acoustic emissions emitted by bubbles entrained in breaking waves (Buckingham and Epifanio, 1997).

### (b) Acoustic emissions from bubble entrainment

In section 7.2.2.5(b) the existence of a bubble pulsation resonance was described, and an approximate resonance relation was stated in equation (7.47). The contributory parameters to that expression are:

$$f_o \approx \frac{1}{2\pi R_o} \sqrt{\frac{3\gamma P_o}{\rho_o}} \quad (7.54)$$

where  $P_o$  is the static pressure. This equation, which assumes adiabatic gas compression and ignores surface tension and viscosity, is valid for air bubbles in seawater having radii of greater than about 10  $\mu\text{m}$ . It was first introduced by Minnaert (1933), who experimentally verified the theory by comparing, with his ear, the sounds emitted by bubbles on injection into a water tank with the notes of tuning forks. Minnaert went on to refer to bubble pulsation as the possible source for ‘the murmur of the brook, the roar of the cataract, or the humming of the sea’. The acoustic signal generated by each bubble is an exponentially decaying sinusoid of the natural frequency, reflecting the bubble’s lightly damped oscillator character. (In fact bubbles oscillating collectively in a cloud can also generate signals at frequencies much less than their individual resonances (Carey, 1987; Prosperetti, 1988; Roy *et al.*, 1992).) A series of these, recorded from a brook, can be seen in Fig. 7.20, each event representing the entrainment of a single bubble. How such emissions can be exploited as sensors will now be discussed.

#### (i) Acoustic sensing of rainfall over the ocean

The underwater sound from rainfall over the oceans might be used for weather sensing. This technique is particularly useful for remote sensors, when the expense of routing a ship through an area, or the interference of the land mass on island-mounted weather gauges, make those techniques unsuitable. Laville *et al.* (1991) described the use of underwater sound to measure the rate of rainfall over the ocean as ‘a very promising technique’, and stated that



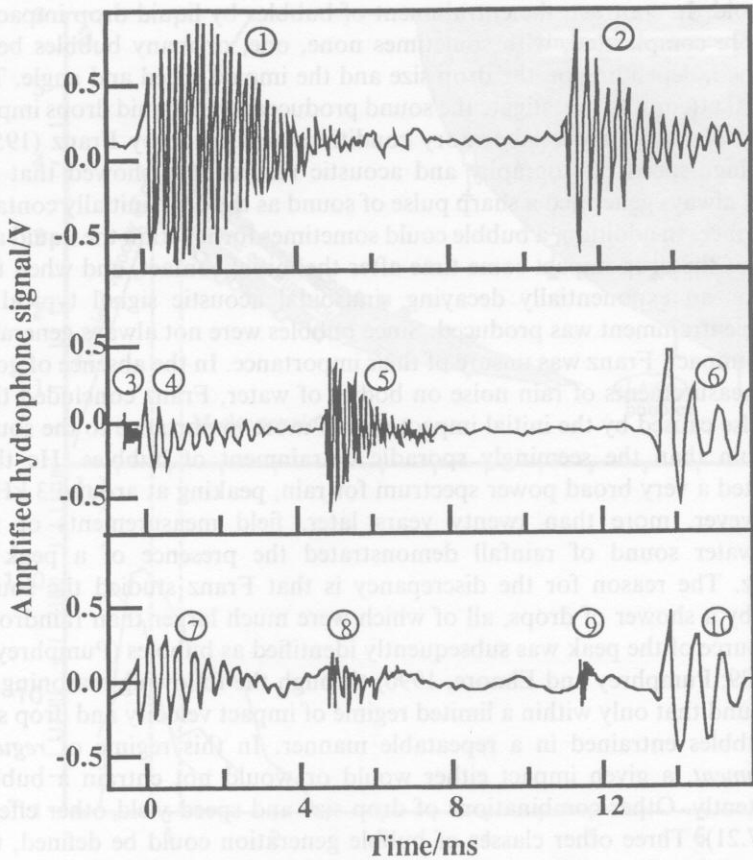


**Figure 7.20** Hydrophone trace from a babbling brook. Ten bubble signatures can be identified, and the bubble size inferred from the natural frequency through equation 7.54.

'local measurements of rainfall rate over large lakes or oceans are needed ... to calibrate global rainfall measurements made from satellites. Above water measurements are inaccurate because of the direct effect of wave action, spray, and wind. Underwater measurements of the sound generated by rainfall are not directly affected by these surface phenomena, which makes them potentially much more accurate.'

In addition, there are applications for 'the remote sensing of rainfall from an underwater location'.

The history of measurement of the underwater sound of rain is described by Leighton (1994, §3.7.2). When a solid sphere impacts a body of water bubbles are entrained provided that the impact speed exceeds a certain



threshold. In contrast, the entrainment of bubbles by liquid drop impact is far more complicated, with sometimes none, one, or many bubbles being entrained, depending on the drop size and the impact speed and angle. The first real attempt to investigate the sound produced when liquid drops impact a body of liquid under laboratory conditions was made by Franz (1959), using high-speed photography and acoustic records. He showed that the impact always generated a sharp pulse of sound as the drop initially contacts the surface. In addition, a bubble could sometimes form within the liquid as a result of the drop impact some time after the initial contact, and when this happens an exponentially decaying sinusoidal acoustic signal typical of bubble entrainment was produced. Since bubbles were not always generated by the impact, Franz was unsure of their importance. In the absence of good field measurements of rain noise on bodies of water, Franz concluded that the pulse caused by the initial impact was of more importance to the sound spectrum than the seemingly sporadic entrainment of bubbles. He thus predicted a very broad power spectrum for rain, peaking at around 3 kHz.

However, more than twenty years later, field measurements of the underwater sound of rainfall demonstrated the presence of a peak at 14 kHz. The reason for the discrepancy is that Franz studied the sound made by a shower of drops, all of which were much larger than raindrops. The source of the peak was subsequently identified as bubbles (Pumphrey *et al.*, 1989; Pumphrey and Elmore, 1990) through the following reasoning. It was found that only within a limited regime of impact velocity and drop size are bubbles entrained in a repeatable manner. In this regime of *regular entrainment*, a given impact either would or would not entrain a bubble consistently. Other combinations of drop size and speed yield other effects (Fig. 7.21). Three other classes of bubble generation could be defined, the regimes being dependent on the drop size and the impact velocity. *Irregular entrainment* involves the production of bubbles through the complex details of the splash. Pumphrey and Elmore also name this 'Franz-type' entrainment because for a given drop diameter and impact velocity in this regime one cannot predict whether or not a bubble will be entrained. *Large bubble entrainment* confines most of the volume of the crater within the bubble. This entrainment might be influenced by surface oscillations on the falling drop. What we now know to be both regular and large bubble entrainment events feature in an article by Jones (1920) who in 1915 observed drops falling into a body of water. He noticed that there were critical ranges of distances through which the drop would fall and produce a characteristic sharp 'click' (which would now be classed as regular entrainment). Occasionally a 'softer, duller sound' occurred, and a bubble was afterwards observed at the point where impact had occurred. This would now be ascribed to large bubble entrainment. Jones observed no bubble remaining behind after the 'click' events, presumably because the regularly entrained bubbles were too small or burst too rapidly for him to detect.

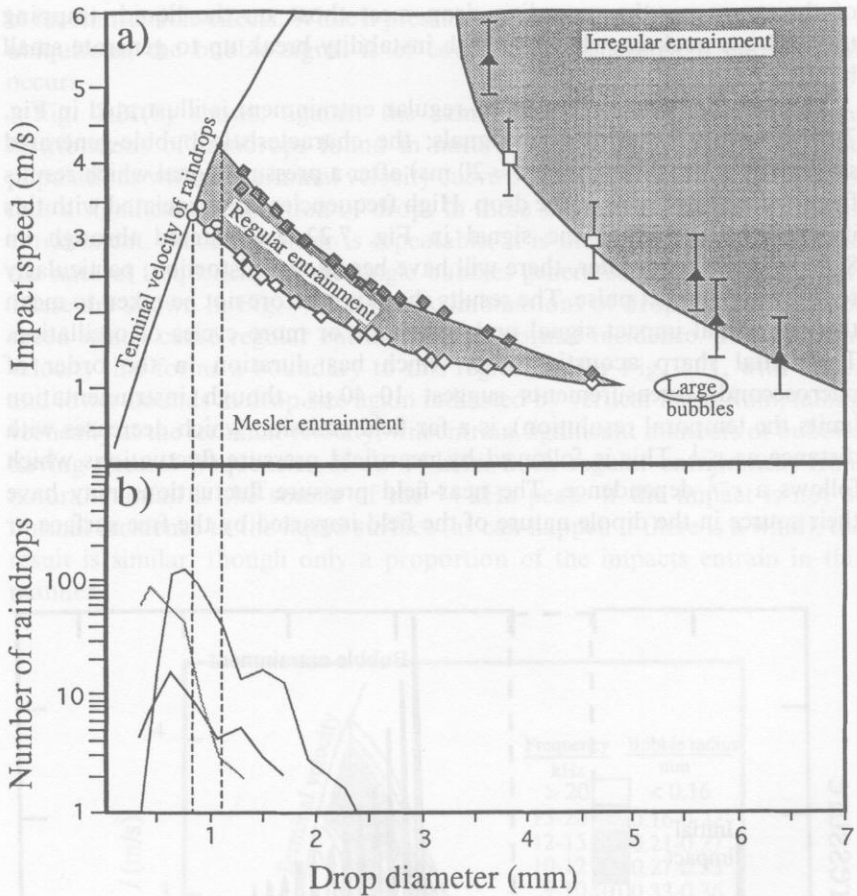


**Figure 7.21** (a) Entrainment regimes (for normal incidence). (b) Typical natural raindrop spectra. Natural rainfall data for three showers, from Scrimger *et al.*, (1987). Entrainment data from Pumphrey and Elmore (1990) (Lower limit, irregular entrainment: solid triangles; lower limit, regular entrainment: open circles). All other data points from Pumphrey (1989). (after Leighton (1994), by permission of the publisher, Academic Press, London.)

Regular, irregular and large bubble entrainment all generate significant sound. *Mesler entrainment* is generally a low-velocity unpredictable phenomenon which occurs when a multitude of small bubbles ( $R_0 \sim 50 \mu\text{m}$ ) is trapped in the initial stages of impact. It does not produce significant acoustic emission. The gas pockets may perhaps be trapped in the troughs of capillary waves which spread out from the point of contact on both the drop and the surface of the water body (Oğuz and Prosperetti, 1990). The peaks

of the waves on the spreading drop meet those on the liquid, trapping toroidal gas pockets, which through instability break up to generate small bubbles.

The pressure field generated by regular entrainment is illustrated in Fig. 7.22. There are two distinct signals; the characteristic bubble-generated sinusoid is emitted some time ( $\approx 20$  ms) after a pressure signal which results from the initial impact of the drop. High frequencies are associated with this initial impact, and as the signal in Fig. 7.22 was filtered through an 8–50 kHz bandpass filter, there will have been some distortion, particularly to the initial impact pulse. The results should therefore not be taken to mean that the initial impact signal undergoes one or more cycles of oscillation. The initial sharp acoustic pulse, which has duration in the order of microseconds (measurements suggest 10–40  $\mu$ s, though instrumentation limits the temporal resolution), is a far-field emission which decreases with distance as  $r^{-1}$ . This is followed by near-field pressure fluctuations which follows a  $r^{-2}$  dependence. The near-field pressure fluctuations may have their source in the dipole nature of the field imparted by the free surface or

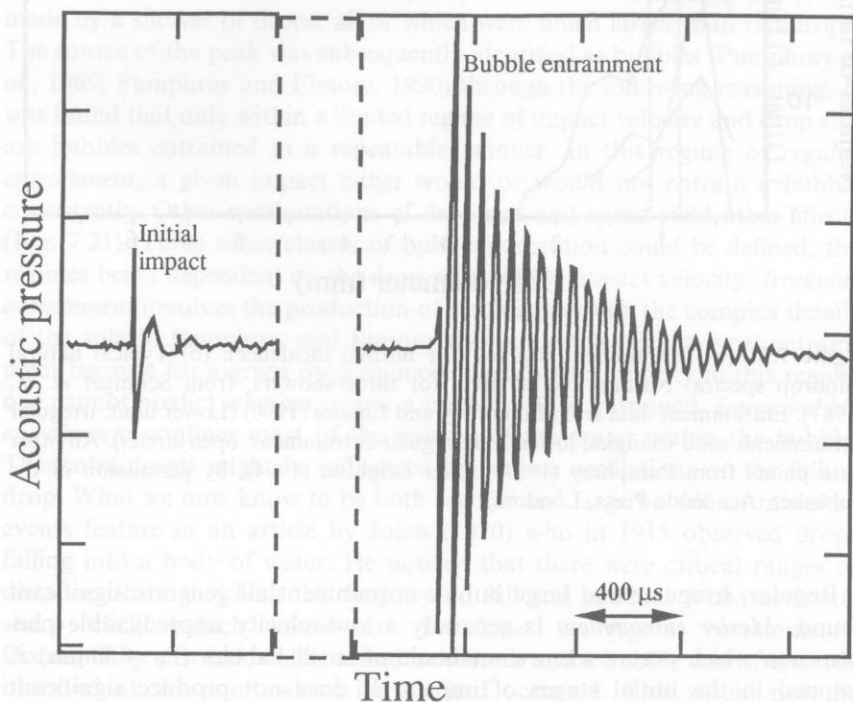


**Figure 7.22** A hydrophone trace showing the underwater pressure signal emitted by a regular entrainment (after Medwin *et al.*, 1990).

in incompressible effects. While a pressure emission from the initial impact is ubiquitous, the bubble signal is of course only generated if entrainment occurs.

Fig. 7.21(b) shows, against the same drop diameter scale, the size distributions of raindrops found in natural rainfall. By comparing these populations with the terminal velocity curve plotted in Fig. 7.21(a), it is clear that a significant proportion of drops in these showers might cause regular entrainment. Since the latter is repeatable, it is then possible to determine the natural frequencies of the single bubbles generated by each such event. These are shown in Fig. 7.23 for the combinations of drop size and impact speed which cause regular entrainment at normal incidence. The terminal velocity line forms a boundary to this region, as for Fig. 7.21, with upper and lower bounds in drop size again indicated by vertical lines. Rain, falling vertically at the terminal velocity, will entrain significant numbers of bubbles having natural frequencies of 12–14 kHz. Such regular entrainment from natural rainfall is the source of the 14 kHz peak. If the impact is not at normal incidence to the liquid surface (as can happen if there is a wind), the result is similar, though only a proportion of the impacts entrain in this manner.

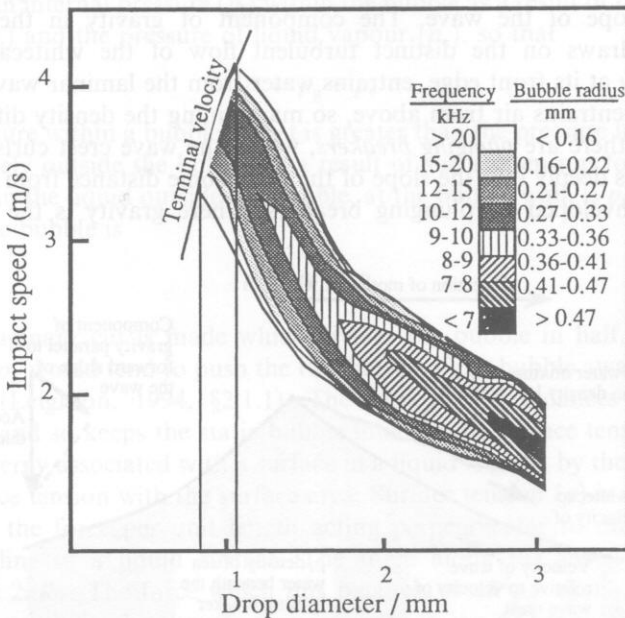


**Figure 7.23** For regular entrainment at normal incidence, certain combinations of drop size and speed entrain bubbles of specific size, such that 12–14 kHz would not be unexpected from natural rain (after Pumphrey and Elmore, 1990).

## (ii) Bubbles in breaking waves

The oceans act as a huge reservoir of gas into which atmospheric gases can dissolve on a global scale. By conservative estimates, 1000 million tonnes of atmospheric carbon dissolve into the seas each year. Of particular climatic significance are the atmosphere/ocean fluxes of carbon dioxide and dimethylsulphide. Bubbles clearly introduce an asymmetry into the flux. On formation through wave action, they trap atmospheric gas, and through dissolution pump it into the sea. The effect of bubbles is likely to be more important in the flux of gases which are less readily soluble in water than carbon dioxide.

Several types of breaking wave can be identified. *Surging breakers*, which develop as a wave runs up on a steep beach, are restricted to shallow waters. However two forms of breaker are not. First there are *spilling breakers*, where the broken water seems to develop more gently from an instability at the sharp crest and forms a quasi-steady whitecap on the forward slope (Fig. 7.24). Because of the presence of a significant number of air bubbles, trapped as the wave breaks gently at the crest, the whitecap is lighter than the water below. The density difference inhibits mixing with the face of the wave, and the whitecap rides on top of the sloping sea surface, retaining its identity. Longuet-Higgins and Turner (1974) proposed that a spilling breaker can be regarded as a turbulent gravity current riding down the forward slope of the wave. The component of gravity in the relevant direction draws on the distinct turbulent flow of the whitecap which, particularly at its front edge, entrains water from the laminar wave surface below and entrains air from above, so maintaining the density difference.

Second, there are *plunging breakers*, where the wave crest curls forward and plunges deeply into the slope of the wave some distance from the crest. Whether enveloped by plunging breakers (where gravity is the restoring

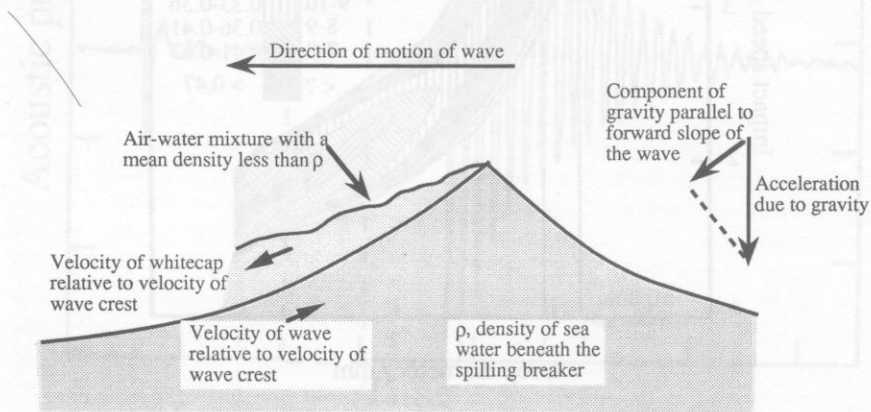


Figure 7.24 Model of a spilling breaker (after Longuet-Higgins and Turner, 1974, by permission of Cambridge University Press).



force for the wave motion), or trapped in troughs in steep capillary (where surface tension acts as the restoring force) or capillary-gravity waves, one might envisage the resulting pockets of air to resemble horizontal cylinders. Longitudinal instabilities would cause each cylinder to fragment along its length, eventually to form a number of roughly spherical bubbles. Fragmentation through shape oscillation might also occur (Longuet-Higgins, 1990; Leighton *et al.*, 1995).

The fact that a bubble, upon entrainment, 'rings' at its natural frequency indicates an exciting impulse is delivered at that time. This impulse can come from a number of sources (Leighton, 1994, §3.7.3). Two, the surface tension and hydrostatic pressures, are particularly interesting. This is because the impulse is delivered in the form of an overpressure which, in the short term, causes the newly formed bubble to be compressed towards the equilibrium radius. The overshoot of this motion sets up the oscillation and consequently generates the acoustic emission. However in the long term, it is such overpressures which drive the gas contained within the bubble into solution.

Surface tension tends to create a compressive force on a spherical bubble. This effect produces the so-called Laplace pressure ( $p_\sigma$ ), which contributes to the degree by which the pressure of the gas in the bubble tends to exceed the pressure in the surrounding liquid. Consider the bubble of radius  $R$ . There is an internal pressure ( $p_i$ ) within the bubble as a result of the pressure of gas ( $p_g$ ) and the pressure of liquid vapour ( $p_v$ ), so that

$$p_i = p_g + p_v . \quad (7.55)$$

The pressure within a bubble at rest is greater than the pressure in the liquid immediately outside the bubble as a result of surface tension forces. If the pressure in the liquid outside the bubble, at the bubble wall, is  $p_L$ , then that within the bubble is

$$p_i = p_L + p_\sigma . \quad (7.56)$$

If an imaginary cut is made which divides the bubble in half, the excess pressure  $p_\sigma$  would tend to push the two halves of the bubble away from one another (Leighton, 1994, §2.1.1). The force which balances the excess pressure and so keeps the static bubble intact is the surface tension.

The energy associated with a surface in a liquid is given by the product of the surface tension with the surface area. Surface tension ( $\sigma$ ) is numerically equal to the force per unit length acting perpendicular to one side of a straight line in a liquid surface. The force along the imaginary cut is therefore  $2\pi R\sigma$ . The force which this balances is  $\pi R^2 p_\sigma$ , that is the excess pressure multiplied by the effective area seen in the direction of the 'push',  $\pi R^2$ . Equating this to the surface tension force gives

$$p_\sigma = \frac{2\sigma}{R} , \quad (7.57)$$



the excess pressure inside a bubble which results from surface tension, also known as the *Laplace pressure*. This acts in conjunction with the hydrostatic pressure ( $p_h$ ) to generate acoustic emission and gas dissolution. The smaller the bubble, and the shallower its depth, the more significant is the surface tension, as opposed to the hydrostatic, pressure (Leighton, 1994 §3.7.3).

Consider therefore a pocket of gas which is entrained at the ocean surface. Before the liquid meniscus is complete, the gas pressure inside is atmospheric,  $p_{\text{atm}}$  (Fig. 7.25(a),(b)). However when the bubble wall is formed, the pressure in the liquid outside the bubble is  $p_{\text{atm}} + p_h$ , where  $p_h = \rho gh$  if  $h$  is the entrainment depth (Fig. 7.25(c)), so that the equilibrium condition of the bubble would have the internal pressure ( $p_i$ ) such that

$$p_i = p_g + p_v = p_\sigma + \rho gh \quad (7.58)$$

Immediately after entrainment the gas pressure equals  $p_{\text{atm}}$ , which is less than that required for equilibrium. Therefore the bubble must compress towards equilibrium, and overshoot results in oscillation. Similarly if the level of gas dissolved in the seawater is in equilibrium with the atmosphere, then it will not be in equilibrium with the gas pressure within the bubble when these oscillations have damped down; the bubble will dissolve, and a supersaturation may result.

#### 7.2.3.2 Non-bubble sources of ambient noise

Knudsen *et al.* (1948) summarized much Second World War data by characterizing the undersea noise in the frequency range 100 Hz to 25 kHz. Wenz confirmed these so-called 'Knudsen spectra', and commented that wind-dependence between 50 Hz and 10 kHz could be caused by air bubbles. The Knudsen spectrum can conveniently be divided into three parts. There is a dominant low-frequency component below 50 Hz, a shipping component at intermediate frequencies, and above 100 Hz one which peaks at 500 Hz, then falls off at  $\sim 6$  dB per octave. At windspeeds greater than  $\sim 5$  m/s, whitecaps are extensively present and the Knudsen

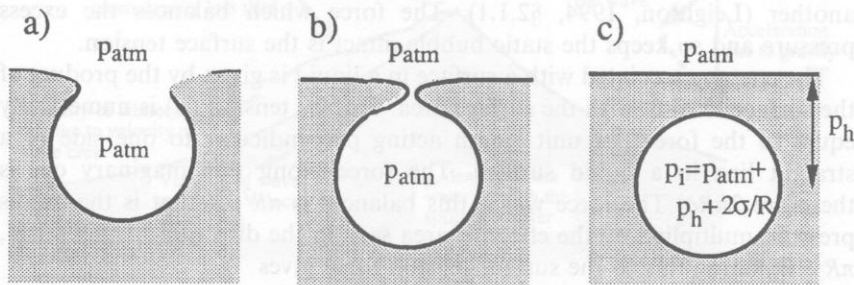


Figure 7.25 The gas pressures associated with bubble entrainment.

spectrum originates from breaking waves. However the Knudsen spectrum can still be detected at windspeeds as low as 1 m/s. The main non-bubble sources of ambient noise are detailed in the references given at the start of the chapter, and briefly outlined below. It should be noted that, in the term 'ocean ambient noise', the 'noise' need not be acoustic. It may for example arise through vibration, electrical, pyroelectric and two types of non-acoustic pressure changes; turbulent and hydrostatic

Hydrostatic pressure changes at receivers can be caused by tides (1–2 cycles/day), which can also contribute to flow noise and can occur at sensor supports. Though wave motion can change the water head above a sensor, the pressure fluctuations do not propagate to depth unless a nonlinear process associated with the surface standing waves occurs. Continuous microseisms contribute noise at around 1/7 Hz, and intermittent acoustic emissions can be generated by earthquakes, volcanoes, etc. Dynamic pressure fluctuations can arise at sensors as a result of ocean turbulence. Low frequencies (below  $\sim 500$  Hz) from ships and storms can propagate to long distances. Significant biological noise can be generated by three groups of marine animals. Some fish can emit sound; frequently cited are the croakers of Chesapeake Bay, which drum air bladder muscles. Some Crustacea (shellfish) can make noise (e.g. the claws of snapping shrimp can generate sound in the range 500–20 000 Hz). The echo-location emissions from whales, dolphins, and porpoises were mentioned earlier, and communication can also be achieved. It is now thought that the mysterious '20-cycle pulse' is generated by the Finback whale (Premus and Spiesberger, 1997). The 20 Hz tone-bursts comprises a pulse every 10 seconds, of 1 s duration, detected for several minutes (6–25 min) by bottomed hydrophones in the Atlantic and Pacific Oceans. This is followed by 2–3 mins of silence. The signal repeats, for many hours. Triangulation shows that the sources move randomly at 2–3 knots, and are high power (1–25 W), and therefore detectable 35 miles away in shallow continental shelf water.

Ambient noise in shallow water is variable in space and time. Sources include noise from wind, shipping, industrial and biological sources. In addition, deep water noise may propagate over distances into shallow waters.

### 7.3 NONLINEAR UNDERWATER ACOUSTICS

As sources of higher power were developed, and as our ability to analyse and process acoustic signals improved, it became clear that the description of simple linear acoustics is inadequate to explain many phenomena associated with the propagation of sound of finite amplitude. Though less amenable to simple explanation, these nonlinear phenomena have over the past few decades proved a valuable area of research. Returns have included the parametric array, which is a form of nonlinear sonar, the enhanced resolution of acoustic microscopes, and the application of the nonlinear

properties of tissue for diagnostic and therapeutic purposes. Though such uses have only appeared in the last few decades, it has been the subject of consideration since the eighteenth century. Probably the first discussions were published in 1759 by Euler, who considered the nonlinear wave equation for finite-amplitude sound.

### 7.3.1 Nonlinear propagation of waves of finite amplitude

In Chapter 1, a derivation was given of the linearized wave equation in acoustic pressure,  $p$ :

$$\nabla^2 p = \frac{1}{c^2} \ddot{p} . \quad (7.59)$$

Any variable which satisfies the linearized wave equation will propagate as a waveform without loss through an ideal medium. In order for the acoustic pressure to satisfy the linearized wave equation, the above derivation requires the assumptions that fluid particle velocity fluctuations are very much less than the speed of sound in the liquid, and also that density fluctuations are negligible in comparison with the equilibrium density. Obviously density is not constant during the propagation of an acoustic wave. Particle displacements cause local variations in density which are periodic for a sinusoidal wave. Therefore the meaning of this derivation is that the smaller the amplitude of the acoustic wave, the more nearly it approximates to the case of the linear waves discussed in Chapter 1. Finite-amplitude sound waves will propagate in a fluid, but their physics is more complicated.

The same argument can be followed mathematically (Leighton, 1994, §1.2.3). The characterization of the propagation of an acoustic wave in a fluid requires three fundamental inputs enshrined in equations reflecting: first, the motion of mass in a fluid; second, the fluid dynamic properties relating such motions to the pressure gradient which causes them, as observed from a frame which moves along with an element of fluid in the flow; and third, an equation of state. This is a thermodynamic equation, the input from which is introduced into this proof from section 1.3. Stated in one-dimensional form, these three equations, are, as follows. First, the equation of continuity (see Chapter 1).

$$\frac{\partial \rho}{\partial t} + \frac{\partial(\rho u)}{\partial x} = 0 \Rightarrow \frac{1}{\rho} \frac{\partial \rho}{\partial t} + \frac{\partial u}{\partial x} + \frac{u}{\rho} \frac{\partial \rho}{\partial x} = 0 \quad (7.60)$$

where  $u$  is the particle velocity;

Second, Euler's equation for an inviscid fluid:

$$\frac{\partial P}{\partial x} + u \rho \frac{\partial u}{\partial x} + \rho \dot{u} = 0 \quad (7.61)$$

where  $P$  the total pressure.

Third, following equations (1.4), (1.5) and (1.10) from section 1.3:

$$c^2 = \partial P / \partial \rho \quad (7.62)$$

(where  $\partial P / \partial \rho = \partial p / \partial \rho$  if the only fluctuating component of the total fluid pressure is the acoustic one). Combination of these three equations allows formulation of the propagation of acoustic longitudinal waves in a fluid, as now follows. The relationship

$$\frac{\partial \rho}{\partial t} c^2 = \frac{\partial P}{\partial t} \quad (7.63)$$

which is derived from equation (7.62), can be substituted into the expanded form of equation (7.60) so that the term  $(\partial \rho / \partial t) / \rho$  converts into  $(\partial P / \partial t) / (\rho c^2)$  to give:

$$\frac{\partial u}{\partial x} + \frac{u}{\rho} \frac{\partial \rho}{\partial x} + \frac{1}{\rho c^2} \dot{P} = 0 \quad (7.64)$$

If the nonlinear terms  $u\rho(\partial u / \partial x)$  and  $(u/\rho)(\partial \rho / \partial x)$  are negligible, equations (7.61) and (7.64) reduce, respectively, to

$$\frac{\partial p}{\partial x} + \rho_0 \dot{u} = 0 \quad (7.65)$$

and

$$\frac{\partial u}{\partial x} + \frac{1}{\rho_0 c^2} \dot{P} = 0 \quad (7.66)$$

where the approximations  $\dot{P} = \dot{p}$  and  $\partial P / \partial x = \partial p / \partial x$  are justified if the only varying component of the total pressure is the acoustic one. The introduction of  $\rho_0$ , the equilibrium fluid density, is appropriate since the second of the two assumptions made after equation (7.64) is that the proportional changes in density with position are negligible. Equations (7.65) and (7.66) combine to give the linearized wave equation by differentiating equation (7.65) with respect to  $x$ , and differentiating equation (7.66) with respect to  $t$ , and then equating the terms  $\partial^2 u / (\partial t \partial x)$  and  $\partial^2 u / (\partial x \partial t)$  between them to give the linearized wave equation in one dimension:

$$\frac{\partial^2 p}{\partial x^2} - \frac{1}{c^2} \frac{\partial^2 p}{\partial t^2} = 0 \quad (7.67)$$

which describes a pressure wave propagating at speed  $c$ . If however the nonlinear terms  $u\rho(\partial u / \partial x)$  and  $(u/\rho)(\partial \rho / \partial x)$ , which were assumed to be negligible after equation (7.64), cannot be neglected, then equation (7.67) cannot be produced from the fundamental three equations. This occurs when proportional changes in density and  $\partial u^2 / \partial x$  are not small, which tends to occur as the wave amplitude increases. This is why equation (7.67) is said

to refer to the propagation of waves of infinitesimal amplitude. The wave is termed 'finite amplitude' when its propagation deviates from the simple longitudinal case described in much of Chapter 1. This has two important effects when the propagation of a sinusoidal acoustic wave is considered.

First, there is a *convection* effect. In simple terms, if  $u/c$  is not negligible, then parts of the wave tend to propagate as  $c + u$ . The particle velocity varies throughout the wave, and so since particle velocity and acoustic pressure are in phase for such a wave (Chapter 1), the greater the local acoustic pressure, the greater the velocity of migration of that section of the wave. Therefore regions of compression tend to migrate faster than the regions of rarefaction (where  $u$  is opposite to  $c$ ). The pressure peak travels with the greatest speed, the trough with the least.

Second, there is an effect which arises because, when a fluid is compressed, its bulk modulus increases. This causes an increase in sound speed, and this effect too will cause the pressure peaks to travel at greater speed than the troughs, and tend to try to catch up and encroach upon them. A continuous wave that is initially sinusoidal will therefore distort in the way shown in Fig. 7.26. The sketches illustrate the shape of a single cycle which is part of a long wavetrain of identical cycles. The plot shows the pressure as a function of distance. The cycle is initially sinusoidal, and its spectral content (shown on the right) is narrowly distributed around a single frequency (since the wavetrain is long, but not infinite). (i) As it propagates through the medium, each compressive region gains upon the preceding rarefactive half-cycle, an accumulated steepness of the waveform between the two developing. Harmonics of the frequency associated with the initial sinusoid appear in the spectrum (see section 7.3.4). (ii) After propagating a certain distance (the *discontinuity length*), the waveform includes a discontinuity; a shock wave develops, as shown in the figure by the discontinuity in the spatial pressure profile, with an associated continuum in the spectrum. (iii) With increasing time, any further compressional advance leads to dissipation and results in a reduction in the amplitude of the shock. This is because the waveform distortion has been equivalent to transferring some of the energy of the initial wave to higher frequencies, which are more strongly absorbed (section 7.2.2.4(b)). (iv) The energy transfer is not sufficient to maintain the shock, and the wave approaches a low-amplitude sinusoidal form (termed 'old age').

An additional feature, not shown in the schematic in Fig. 7.26, arises from the action of dissipation and diffraction, which cause phase shifts in the various frequency components of the wave. As a result, the distorted waveform is not symmetrical about the zero-line. In general the trough, which corresponds to negative values of the acoustic pressure, becomes rounded while the positive peak is augmented.

As outlined above, there are two contributions to the change in phase speed of the wave, the change in stiffness (or bulk modulus) and the convection. These are called the *material nonlinearity* and the *convective*



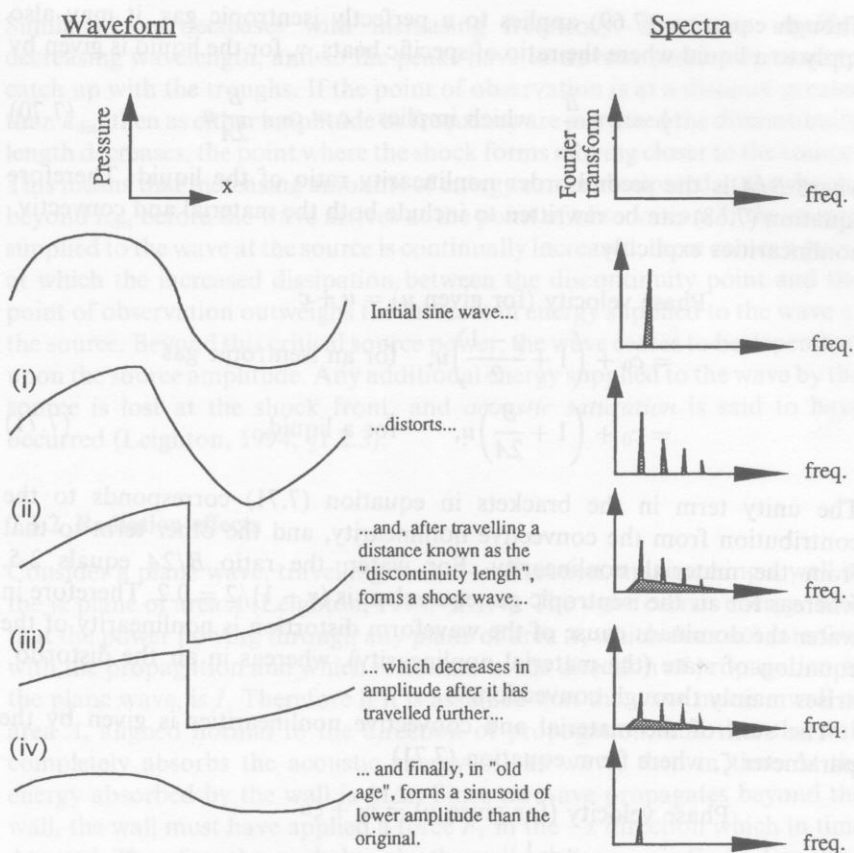


**Figure 7.26** The waveforms and associated spectra relevant to this example of the non-linear propagation of finite-amplitude, initially sinusoidal, waves. The figure shows one example cycle out of an infinite wavetrain of single frequency.

*nonlinearity* respectively, and are formulated as follows (Leighton, 1994, §1.2.3). The phase velocity of a point in the wave having particle velocity  $u$  is

$$\text{Phase velocity (for given } u) = u + c \quad (7.68)$$

where a convection component  $u$  is added to  $c$ , the local speed of sound. This local speed has in turn been affected by the change in bulk modulus, and is related to  $c_0$ , the sound speed for waves of infinitesimal amplitude, by

$$c = c_0 + \frac{\gamma - 1}{2} u \quad (7.69)$$



Though equation (7.69) applies to a perfectly isentropic gas, it may also apply to a liquid where the ratio of specific heats,  $\gamma$ , for the liquid is given by

$$\gamma = 1 + \frac{B}{A} \quad \text{which implies} \quad c = c_0 + \frac{B}{2A}u \quad (7.70)$$

where  $B/A$  is the second-order nonlinearity ratio of the liquid. Therefore equation (7.68) can be rewritten to include both the material and convective nonlinearities explicitly:

$$\begin{aligned} \text{Phase velocity (for given } u) &= u + c \\ &= c_0 + \left(1 + \frac{\gamma - 1}{2}\right)u, \quad \text{for an isentropic gas} \\ &= c_0 + \left(1 + \frac{B}{2A}\right)u, \quad \text{for a liquid.} \end{aligned} \quad (7.71)$$

The unity term in the brackets in equation (7.71) corresponds to the contribution from the convective nonlinearity, and the other term to that from the material nonlinearity. For water, the ratio  $B/2A$  equals 2.5, whereas for air the isentropic gas equivalent is  $(\gamma - 1)/2 = 0.2$ . Therefore in water the dominant cause of the waveform distortion is nonlinearity of the equation of state (the material nonlinearity), whereas in air the distortion arises mainly through convection.

The sum of the material and convective nonlinearities is given by the parameter  $\zeta$ , where from equation (7.71)

$$\begin{aligned} \text{Phase velocity (for given } u) &= c_0 + \zeta u \\ \text{where } \zeta &= \frac{\gamma + 1}{2}, \quad \text{for an isentropic gas, and} \\ \text{where } \zeta &= \left(1 + \frac{B}{2A}\right), \quad \text{for a liquid.} \end{aligned} \quad (7.72)$$

For air  $\zeta = 1.2$ , and for water  $\zeta = 3.5$ . From this one might expect the distortion to be more obvious in water than in air; however one must take into account attenuation of high frequencies. The discontinuity length, which is taken to be the distance propagated when an infinite slope first appears in the waveform, is given by

$$L_{\text{dis}} = \frac{1}{\zeta M k}, \quad (7.73)$$

where  $k = \omega/c_0$  and where  $M$  is the peak acoustic Mach number of the source, the ratio of the amplitude of the particle velocity at the source to  $c_0$ . Thus the shock forms closer to the source as the coefficient  $\zeta$ , which indicates the degree of nonlinearity, increases. It also forms sooner as the amplitude increases because the speed differential between the peaks and the troughs increases.

Similarly  $L_{\text{dis}}$  decreases with increasing frequency, since this signifies decreasing wavelength, and so the peaks have to travel a shorter distance to catch up with the troughs. If the point of observation is at a distance greater than  $L_{\text{dis}}$ , then as either amplitude or frequency are increased the discontinuity length decreases, the point where the shock forms moving closer to the source. This means that increasing amounts of energy can be dissipated at the shocks beyond  $L_{\text{dis}}$  before the wave arrives at the point of observation. If the energy supplied to the wave at the source is continually increased, there comes a point at which the increased dissipation between the discontinuity point and the point of observation outweighs the increase in energy supplied to the wave at the source. Beyond this critical source power, the wave ceases to be dependent upon the source amplitude. Any additional energy supplied to the wave by the source is lost at the shock front, and *acoustic saturation* is said to have occurred (Leighton, 1994, §1.2.3).

### 7.3.2 Radiation effects

Consider a plane wave, travelling in the  $+x$  direction, approaching a wall in the  $yz$  plane of area  $A$  (Leighton, 1994, §1.1.4). The wave carries energy, such that the power flowing through any plane of area  $A$ , which does not interfere with the propagation and which is normal to the direction of propagation of the plane wave, is  $I$ . Therefore if it is assumed that the wave meets a wall of area  $A$ , aligned normal to the direction of propagation, and that the wall completely absorbs the acoustic energy of the wave, then in time  $\Delta t$  the energy absorbed by the wall is  $IA\Delta t$ . Since no wave propagates beyond the wall, the wall must have applied a force  $F_r$  in the  $-x$  direction which in time  $\Delta t$  acted. Therefore the work done by the wall on the wave is  $F_r c \Delta t$ . Equating this to the energy absorbed, we obtain  $F_r = (IA/c)$ . From Newton's third law of motion, this must be equal and opposite to the force exerted by the wave on the wall. Therefore upon absorption the wave exerts a time-averaged *radiation pressure* in the direction of its motion of magnitude

$$p_{\text{rad,abs}} = \frac{I}{c} \quad (7.74)$$

for normal incidence of plane waves. (Demonstrations of radiation pressure are not confined to acoustics laboratories, but can frequently be seen in science fiction films, where ray guns appear to have the ability to impart a force capable of making the victim stagger backwards. Liking this motion to that observed when catching a 5 kg bag of potatoes, suggests the radiation force is 50 N, so that during firing the ray gun would need to project power  $W$  equal, from equation (7.74), to  $(50c)$  N, where  $c$  is the wavespeed. Were the ray-gun to project electromagnetic radiation, such as a laser beam, the power of the gun would have to be  $50 \times 3 \times 10^8 = 1.5 \times 10^{10}$  W. This is more than ten times the  $1.2 \times 10^9$  W power output of a typical nuclear power station.

However since the speed of sound is lower than that of light, the equivalent power requirements would be 17 kW in air and 75 kW in water.) The force  $F_r$  exerted by the wall can also be thought of as acting upon the wave to absorb its momentum. In time  $\Delta t$ , the wall absorbs a length  $L = c\Delta t$  of the wave, exerting an impulse  $F_r\Delta t = IAL/c^2$  upon the wave, causing a change in momentum of  $\Delta J$ . Since after absorption the momentum of wave is zero, then the momentum associated with one wavelength of the wave is

$$J_\lambda = \frac{IA\lambda}{c^2} \quad (7.75)$$

If the wave is reflected, instead of being absorbed, this momentum must be not simply absorbed but reversed. The wall must exert twice as much force upon the wave, and so the time-averaged radiation pressure felt by the reflector is

$$p_{\text{rad,refl}} = \frac{2I}{c} \quad (7.76)$$

for total reflection of normally-incident waves back along the line of incidence (Leighton, 1994, §1.1.4).

As the acoustic wave travels through a medium, it will be absorbed to a certain extent (section 7.2.2.4(b)). However the momentum absorbed from the acoustic field manifests as a flow of the liquid in the direction of the sound field, termed *acoustic streaming* (Leighton, 1994, §1.2.3). The above process can also be thought of as the setting up of an energy gradient in the direction of propagation, occurring because energy is absorbed from the beam during its passage through an attenuating liquid. A gradient in energy corresponds to a force, and in general such energy gradients will act upon a liquid causing a streaming flow. The force per unit volume,  $F/V$ , equals the gradient in pressure,  $\nabla p$ , which results in a liquid acceleration in the direction of propagation. In the above case of a beam propagating through an absorbing liquid, the pressure gradient equals:

$$\nabla p = \frac{F}{V} = \frac{2I\alpha}{c} \quad (7.77)$$

From this equation it is clear that if both intensity and attenuation can vary spatially throughout a sound beam in a uniform medium, then so will the streaming forces and flows. An increase in either parameter will increase the streaming. As will be evident from the preceding section, the pumping of energy into higher frequencies, which are more strongly absorbed than the fundamental, means that attenuation may vary spatially in an acoustic field of finite amplitude. Finite-amplitude effects will also affect streaming through the formation of shocks. Starrit *et al.* (1989) observed the enhancement of streaming in high-amplitude diagnostic pulsed ultrasonic fields which have formed shocks in water. Streaming speeds of up to around 10 cm/s can be demonstrated from clinical ultrasonic equipment.

There is a second type of streaming. In contrast to the above examples, this is not associated with bulk flows resulting from energy gradients within the medium through which the sound propagates. Instead, it appears as circulations which occur near small obstacles placed within a sound field, or near small sound sources, or vibrating membranes or wires (Leighton, 1994). It arises from the frictional forces between a boundary and a medium carrying vibrations of circular frequency  $\omega$ , and unlike the streaming described earlier, this time-independent circulation occurs only in a small region of the fluid, being generally confined to an acoustic boundary layer of thickness

$$L_{\text{ms}} = \sqrt{2\eta/\rho\omega} \quad , \quad (7.78)$$

where  $\eta$  and  $\rho$  are the shear viscosity and density respectively of the liquid. Because of the restricted scale of the circulation (often but not exclusively microscopic), it is commonly termed *microstreaming*. Microstreaming can bring about a number of important effects. The shear forces set up within the liquid may disrupt DNA (deoxyribonucleic acid), disaggregate bacteria, disrupt human erythrocytes and platelets *in vitro* and *in vivo*, and other bioeffects. Microstreaming can specifically occur as a result of the oscillations of an acoustically driven bubble in a sound field. As will be discussed in section 7.4.3.2, this can also lead to bioeffects (Leighton, 1994).

### 7.3.3 Self-effects

The nonlinear propagation discussed earlier may be indirectly responsible for the relative scarcity of nonlinear acoustic phenomena, compared to optical ones, as in many pure media sound is non-dispersive at frequencies for which absorption over the distance of a wavelength is small. As a result, high-pressure fields are converted into shock waves as energy is pumped into the higher harmonics, as outlined earlier. Since absorption tends to be greater at higher frequencies, the high frequency oscillations are strongly absorbed, so that strong sound waves are rapidly dissipated in the liquid. This effect can be reduced by engineering dispersion into the medium, for example by propagating the sound through a waveguide, or by introducing gas bubbles. Nevertheless there are several other nonlinear effects associated with the propagation of ultrasound, such as self-interaction and parametric phenomenon, stimulated scattering and phase conjugation (Leighton, 1994, §1.2.3). Examples of some of these are given below.

One self-interaction effect is illustrated by the *self-focusing* of acoustic beams (Fig. 7.27). Thermal self-focusing occurs because, through absorption of acoustic energy, the medium through which the sound beams passes becomes warmer. In most liquids, this causes the sound-speed to fall (or equivalently causes the acoustic refractive index to increase) so that the beam is focused in towards the axis as a result of total internal reflection at its

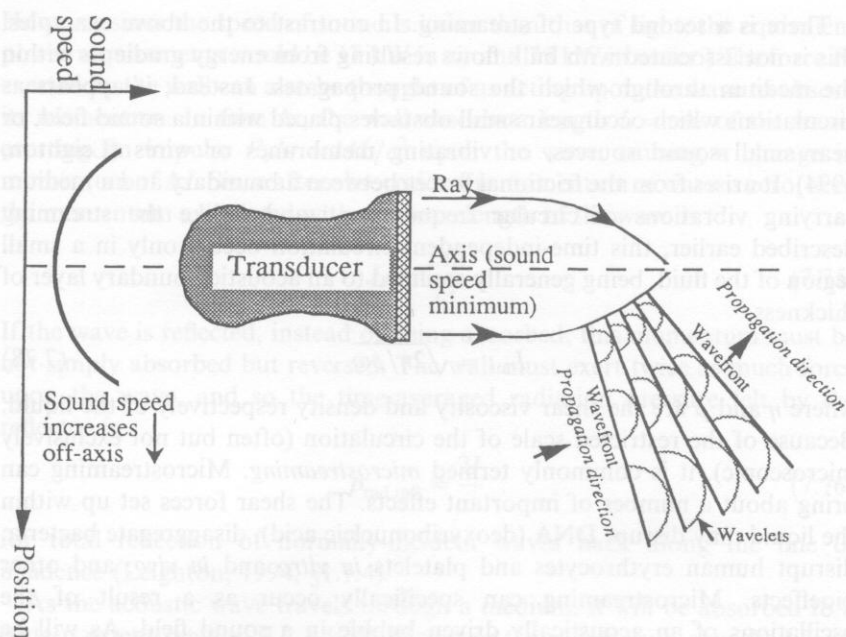


**Figure 7.27** Self-focusing. At the left of the figure, the sound speed profile is shown. Compare with Figs 7.7 and 7.8.

perimeter. In water, however, the sound speed passes through a maximum at 74 °C (Fig. 7.4), so that thermal self-focusing only occurs at temperatures in excess of this. At lower temperatures, the inverse phenomenon of self-defocusing occurs (Fig. 7.28). Acoustic streaming imparts a defocusing effect by increasing the sound speed near the beam axis.

There are mechanisms other than thermal which can bring about self-focusing, including some resulting from the presence of bubbles, which can accumulate on the transducer axis through Bjerknes forces (Leighton, 1994, §4.4.1) and reduce the sound speed there (section 7.2.2.5(b)). The presence of bubbles can also bring about self-transparency, where the absorption decreases with increasing intensity, though this can arise in bubble-free media, such as glycerin, owing to the temperature-dependence of the absorption coefficient.

Self-focusing can occur not just in the bulk of a liquid, but at an interface between two media where, for example, distortion of the surface of a water sample by the beam can lead to a focusing effect simply as a result of local angling of the reflecting surface (Leighton, 1994, §1.2.3). In the extreme case, when the reflected beams are directed upwards, it can lead to *acoustic self-concentration* and the formation of a fountain.



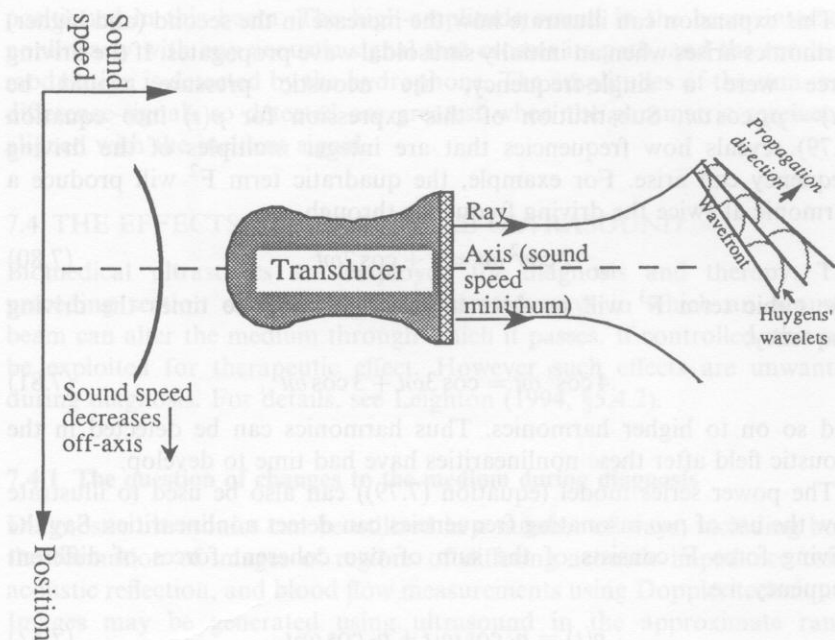


**Figure 7.28** Self-defocusing. At the left of the figure, the sound speed profile is shown. Compare with Figs 7.7 and 7.8.

### 7.3.4 The parametric array

In section 7.3.1, the response (e.g.  $\Delta\rho/\rho$ ) of an element of water to an acoustic wave was considered to be nonlinear at finite amplitude, tending to the linear at infinitesimal amplitudes. Even the simple power series expansion<sup>†</sup> of the force/response relationship illustrates how frequencies other than the driving frequency can arise in such situations in the steady state (a phenomenon which was discussed in that section). In that model, the general response  $\mathbb{Y}(t)$  of the oscillator is a power series of the driving force  $F$ , for example,

$$\mathbb{Y}(t) = s_0 + s_1 F(t) + s_2 F^2(t) + s_3 F^3(t) + s_4 F^4(t) + \dots \quad (7.79)$$

In this circumstance  $\mathbb{Y}$  might stand for the response of the fluid element to pressure. Such a response might be the motion of the fluid element.

<sup>†</sup> Note: The power series expansion given in equation (7.79) is not a complete descriptor of nonlinear oscillation. For example, it will not predict subharmonics. This may be done through Fourier series expansion of the response, or by perturbation methods.

This expansion can illustrate how the increase in the second (and higher) harmonics arises when an initially sinusoidal wave propagates. If the driving force were a single-frequency, the acoustic pressure would be  $p(t) = p_A \cos \omega t$ . Substitution of this expression for  $p(t)$  into equation (7.79) reveals how frequencies that are integer multiples of the driving frequency can arise. For example, the quadratic term  $F^2$  will produce a harmonic at twice the driving frequency through

$$2 \cos^2 \omega t = 1 + \cos 2\omega t . \quad (7.80)$$

The cubic term  $F^3$  will produce a harmonic at three times the driving frequency:

$$4 \cos^3 \omega t = \cos 3\omega t + 3 \cos \omega t , \quad (7.81)$$

and so on to higher harmonics. Thus harmonics can be detected in the acoustic field after these nonlinearities have had time to develop.

The power series model (equation (7.79)) can also be used to illustrate how the use of *two* insonating frequencies can detect nonlinearities. Say the driving force  $F$  consists of the sum of two coherent forces of different frequency, i.e.

$$p(t) = p_1 \cos \omega_1 t + p_2 \cos \omega_2 t , \quad (7.82)$$

where  $\omega_2 > \omega_1$  (the presence of phase constants would not alter the general result). After substituting equation (7.82) into equation (7.79), expansion of the quadratic component contains a term which can be expanded to generate the sum and difference frequencies:

$$2p_2p_1 \cos \omega_1 t \cos \omega_2 t = p_2p_1 \{ \cos(\omega_1 + \omega_2)t + \cos(\omega_2 - \omega_1)t \} . \quad (7.83)$$

The parametric array was conceived in 1960 by Westervelt (1960) and, following examples of applications suggested by Berklay (1965), is now perhaps the most familiar application of nonlinear acoustics. If two collimated acoustic beams of finite amplitude and high frequencies,  $\omega_1$  and  $\omega_2$ , are transmitted in the same direction, nonlinear interaction between them generates sound at  $\omega_c = \omega_1 - \omega_2$ . Thus a parametric antennae, driven at two frequencies, provides a highly directional extended source of low frequency sound. The source itself can be relatively small, and the sidelobe features greatly reduced. The low frequency,  $\omega_c$ , can be detected in the medium, along with such combinations as  $\omega_1 \pm \omega_c$ . However these other frequencies, being higher, are more strongly attenuated and over long propagation distances the lowest frequency,  $\omega_c$ , dominates. The possibility of increasing the efficiency of these systems by the addition of bubbles has been investigated.

Parametric receivers exhibit the same high directionality in the detection of sound. It can be formed from two transducers, one being the source of a collimated acoustic beam of high intensity, and the other a hydrophone

positioned in this beam. The high-amplitude sound in the beam interacts nonlinearly with any acoustic signal that crosses its path, and the resulting modulation is detected by the hydrophone. The amplitudes of the sum- and difference-signals so detected are greatest when the parametric receiver is aligned with the incident signal.

## 7.4 THE EFFECTS OF BIOMEDICAL ULTRASOUND

Biomedical ultrasonics are employed for diagnosis and therapy. The preceding section of this chapter illustrated ways in which an acoustic beam can alter the medium through which it passes. If controlled, this can be exploited for therapeutic effect. However such effects are unwanted during diagnosis. For details, see Leighton (1994, §5.4.2).

### 7.4.1 The question of changes to the medium during diagnosis

Diagnostic ultrasonics can be utilized in a number of ways, including both the formation of images of regions of differing acoustic impedance using acoustic reflection, and blood flow measurements using Doppler techniques. Images may be generated using ultrasound in the approximate range 3–30 MHz, using pulse profiles as shown in Fig. 7.29(a) (the spectrum being shown in 7.29(b)). The pulses are of micro-second order, and the pulse repetition frequency (PRF) is of order 1 kHz. Such technology is used to image major organs (e.g. the heart, gall bladder), the foetus, and abnormal tissues such as tumours and cysts. By 1984 well over a quarter of a million foetuses were exposed to ultrasound annually in Britain alone.

Despite the millions of examinations over the 30 years that diagnostic ultrasound has been used clinically, there is no verified documented evidence of adverse effects in patients caused by exposure to ultrasound. However in the last decade there have been a number of public statements by those advocating caution, and those who attest to the safety, of diagnostic ultrasound. In 1984 Mr John Patten, Junior Health Minister in the United Kingdom, warned against the routine use of ultrasound in pregnancy in a letter to the Association for Improvements in Maternity Services. Quoted in the *Daily Mail* (22 October 1984) and five days later in *Lancet*, he said, 'Given the publicity there has recently been about the possible risk of ultrasound scanning, we would not expect any health authority to be advocating screening for all mothers as a routine procedure.' A debate followed and, for example, Ziskin (1987) commented that 'There is nothing that I'm aware of that has a safer record than that of diagnostic ultrasound.'

Several factors need to be considered. One is the pace of development of the technology. Figure 7.30 shows the trend in output of pulse-echo and Doppler diagnostic equipment. One of the underlying reasons for the trend

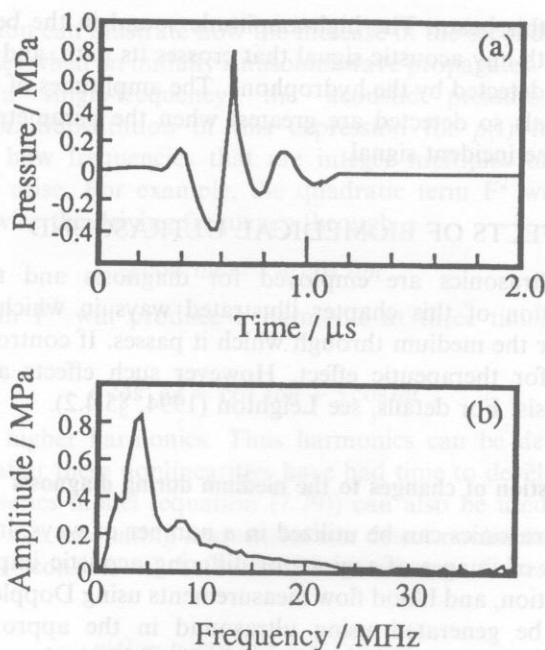


**Figure 7.29** The (a) waveform and (b) spectral magnitudes measured on axis at a distance of 100 mm from transducer faceplate from diagnostic imaging apparatus (after Baker, 1991). Reprinted by permission from *Physics in Medicine and Biology*, 36, 1457–64; copyright © 1991 IOP Publishing Ltd.

to increase intensities and acoustic pressures lies in the tendency for manufacturers to produce diagnostic systems which utilize ever-increasing frequencies, so that the shorter wavelengths will lead to an improvement in resolution. However, since these higher frequencies are more strongly attenuated (section 7.2.2.4(b)), there is an associated tendency to utilize higher acoustic pressures.

The figure also illustrates the need to define the way in which the intensity has been measured. With pulses that may be of microsecond duration but with an inter-pulse time of millisecond order, the time-average acoustic intensity may be three-orders of magnitude less than the temporal peak intensity. Similar comments apply to spatial averaging because often the fields are focused, and the wavelengths are of sub-millimetre order.

Carstensen (1987) states that

‘temporal average intensities in some pulse Doppler devices in use today are close to levels which produce measurable heating of tissues, and the temporal peak pressures in some modern instruments approach the levels of acoustic saturation, i.e. the condition in which nonlinear losses of the

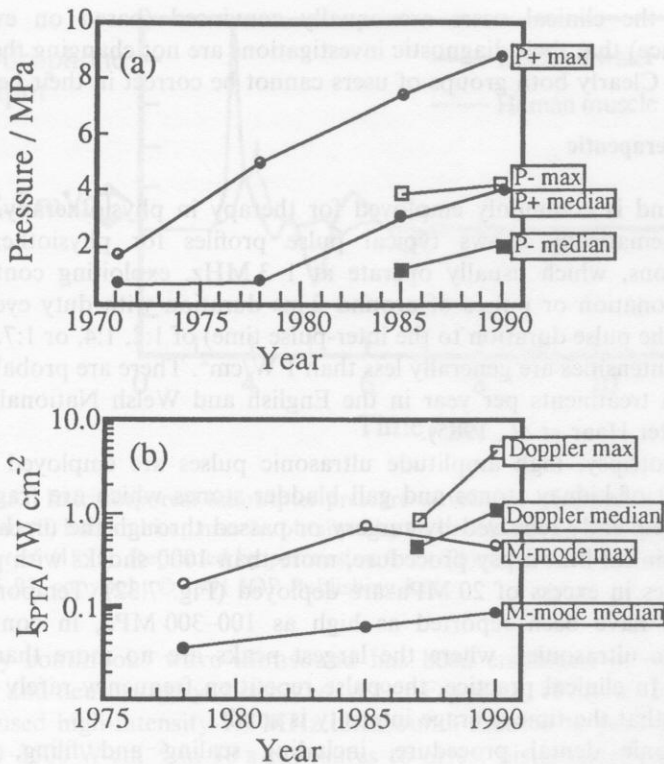


**Figure 7.30** The median and overall maximum outputs from surveys of clinical devices up to 1990. (a) The change in peak negative (labelled 'P-') and peak positive (labelled 'P+') pressures measured in water for pulse-echo diagnostic equipment. (b) The change in  $I_{SPTA}$  (spatial-average, temporal-average intensity), measured in water, for M-mode operation and for pulsed Doppler modes (note that the scale is logarithmic, showing that the maximum from pulsed Doppler has increased roughly ten-fold). After Duck and Martin (1991). Reprinted by permission from *Physics in Medicine and Biology*, **36**, 1423–32; copyright © 1991 IOP Publishing Ltd.

medium set upper limits on local sound source levels regardless of the output from the source.'

Williams (1990) notes that

'the time-averaged intensities emitted by many devices in certain operating modes can exceed the time-averaged intensities to which patients are being subjected during typical physiotherapeutic treatments. We are consequently in a state of confusion where the physiotherapists are convinced (albeit based on tenuous or anecdotal evidence) that their treatments change the functioning of tissues and are therefore efficacious,



while the clinical users are equally convinced (based on even less evidence) that their diagnostic investigations are not changing the tissues at all. Clearly both groups of users cannot be correct in their beliefs.'

### 7.4.2 Therapeutic

Ultrasound is commonly employed for therapy in physiotherapy. Figure 7.31 schematically shows typical pulse profiles for physiotherapeutic applications, which usually operate at 1–3 MHz, exploiting continuous-wave insonation or pulses of around 2 ms duration with duty cycles (the ratio of the pulse duration to the inter-pulse time) of 1:2, 1:4, or 1:7. Spatial average intensities are generally less than  $1 \text{ W/cm}^2$ . There are probably over 1 million treatments per year in the English and Welsh National Health Service (ter Haar *et al.*, 1985).

In lithotripsy, high amplitude ultrasonic pulses are employed for the treatment of kidney stones and gall bladder stones which are fragmented and subsequently removed by surgery or passed through the urethra. In a typical clinical lithotripsy procedure, more than 1000 shocks with pressure amplitudes in excess of 20 MPa are deployed (Fig. 7.32). Temporal peak pressures have been reported as high as 100–300 MPa, in contrast to diagnostic ultrasonics, where the largest peaks are no more than about 10 MPa. In clinical practice, the pulse repetition frequency rarely exceeds 2 Hz, so that the time-average intensity is small.

Ultrasonic dental procedure, including scaling and filing, employ magnetostriction to generate a micrometer order displacement of the tip at 30 kHz. The mechanism of action is through direct physical contact, microstreaming and cavitation. Experiments have investigated treatments involving the application of ultrasound in surgery, where focused, high-

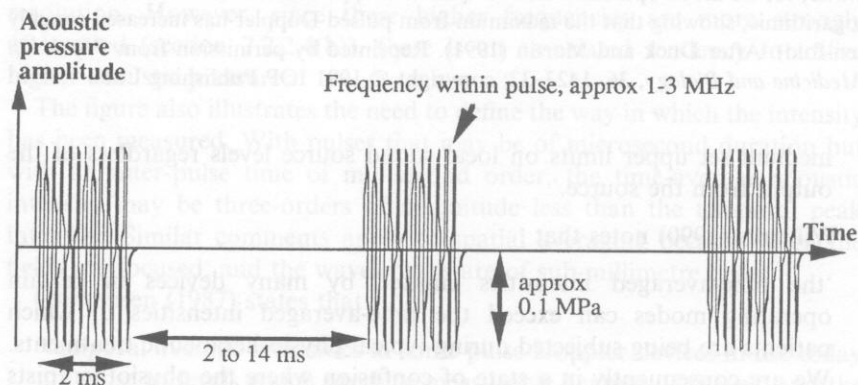
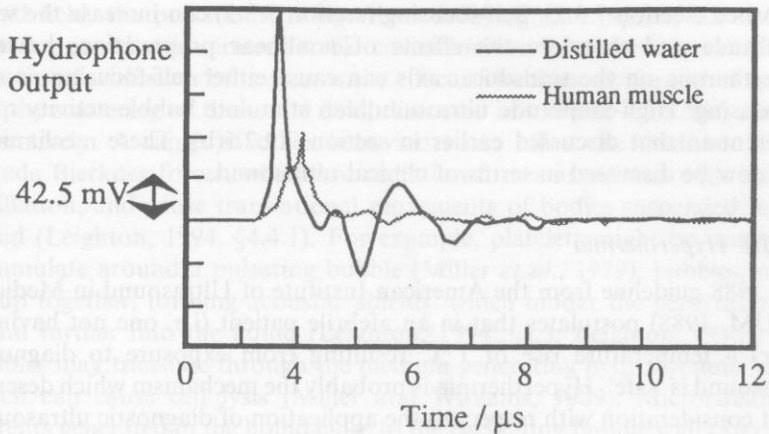


Figure 7.31 Illustration of typical physiotherapeutic output.



**Figure 7.32** Extracorporeal lithotripter pressure waveforms obtained in (i) distilled water, and (ii) human bicep muscle, obtained by an Imotec needle hydrophone. After Finney *et al.* (1991). Reprinted by permission from *Physics in Medicine and Biology*, 36, 1485–93; copyright © 1991 IOP Publishing Ltd.

intensity continuous wave ultrasound has been employed in ophthalmic surgery and neurosurgery (Lizzi *et al.*, 1992; Fry *et al.*, 1970). ter Haar *et al.* (1991) used high-intensity 1.7 MHz ultrasound, focused to peak intensities of  $1400\text{--}3500\text{ W cm}^{-2}$  in 10 s exposures to arrest histologically detectable growth in rat tumours that had been exposed over the whole volume. Wound healing may be promoted by physiotherapeutic-type ultrasound. Other possible effects include a possible placebo effect and phonophoresis, where at frequencies of a few MHz and  $I_{\text{SATA}}$  of order  $1\text{ W cm}^{-2}$  intensities, ultrasound can increase the rate of penetration of a wide range of pharmacologically active agents through the skin. See Leighton (1994, §5.4.2) for details of these various therapies.

### 7.4.3 The mechanisms of bioeffect

A bioeffect may be desired (e.g. in the application of an ultrasonic cell disrupter) or undesired (e.g. during a diagnostic scan). Throughout section 7.3, several mechanisms by which an ultrasonic bioeffect might be brought about have been introduced. These can be interdependent, as the following discussion illustrates. One of the major mechanisms of bioeffect is through hyperthermia, the heating of the medium as a result of the absorption of the acoustic energy (section 7.2.2.4(b)). Such absorption can be enhanced by nonlinear propagation (section 7.3.1). Nonlinear propagation can also enhance streaming by increasing the rate at which the momentum formerly carried by the acoustic wave is transferred into the liquid as the wave is

absorbed (section 7.3.2). Self-focusing (section 7.3.3) can increase the wave amplitude and therefore the effects of nonlinear propagation; however hyperthermia on the transducer axis can cause either self-focusing or self-defocusing. High-amplitude ultrasound can stimulate bubble activity quite different to that discussed earlier in section 7.2.2.5(b). These mechanisms will now be discussed in terms of clinical ultrasound.

#### 7.4.3.1 Hyperthermia

The 1988 guideline from the American Institute of Ultrasound in Medicine (AIUM, 1988) postulates that in an afebrile patient (i.e. one not having a fever) a temperature rise of 1 °C resulting from exposure to diagnostic ultrasound is 'safe'. Hyperthermia is probably the mechanism which deserves most consideration with respect to the application of diagnostic ultrasound. No hazard has been demonstrated *in vivo* with clinical ultrasound.

Experiments show that the biological consequences depend crucially on both the *magnitude* of temperature elevation, and the *duration* of it. The most sensitive tissues are those containing a large proportion of actively-dividing cells (mitosis), and abnormalities can occur in cell division and DNA replication. A wide range of abnormalities have been reported in animals, including retardation of brain changes with reduced learning performance, and low birth weight. For details, see WFUMB (1992, 1994, 1996).

Problems in testing for the effects of hyperthermia include those associated with extrapolating findings from animals to the human case. For example, species have different basal temperature (38.5 °C in rats; 39.5 °C in guinea pigs; 37 °C as in humans). It is not certain whether the absolute temperature, or the temperature increase above normal, is the relevant parameter for hyperthermic bioeffect. If the whole body is subjected to elevated temperatures, as occurs in the air incubators tests which are used in much hyperthermia research, the results may not be directly relevant to the local heating produced by, for example, *in utero* ultrasound. In the latter case, localized heating may be affected by perfusion, whereby blood flow can reduce the temperature rise caused by local heating; and by bone, ultrasonic reflection off which can enhance heating. On the other hand, whole body heating may adversely affect the maternal physiology, or it may be that protective mechanisms, stimulated in response to whole-body heating, do not occur when ultrasound heats locally.

Heating occurs not only through bulk absorption of ultrasound by tissue: losses in the transducer itself cause its temperature to rise, and this must be considered particularly during intracavitary (e.g. endovaginal) applications.

#### 7.4.3.2 Bubble-related mechanisms

In section 7.2.3.1(b), the pulsations of bubbles, decaying in amplitude following their entrainment, was discussed. However when driven by a

sound field, the pulsations, rather than decaying, can persist, the bubble pulsating in what is termed 'stable cavitation' or 'non-inertial cavitation'. Associated with such behaviour is the effect of bubbles on the sound speed, and the scattering of the sound field, discussed in sections 7.2.2.5(b) and (c) respectively. A range of other behaviours can affect the medium. These include Bjerknes forces, which are radiation forces associated with bubble oscillation, and cause translational movements of bodies suspended in the liquid (Leighton, 1994, §4.4.1). For example, platelets might be caused to accumulate around a pulsating bubble (Miller *et al.*, 1979); bubbles might group together, forming acoustic 'shields' which hinder the penetration of sound further into the liquid (Leighton, 1994, §5.3; Leighton, 1995); and bubbles may translate through the medium generating hydrodynamic shear which can cause cell lysis (Miller and Williams, 1989). Microstreaming currents generated in the liquid close to the oscillating bubble wall can cause cell lysis (Vivino *et al.*, 1985). One of the most important effects associated with stable cavitation can be *rectified diffusion* (Leighton, 1994, §4.4.3), where the equilibrium radius of the bubble grows as the pulsations draw previously dissolved gas out from the surrounding liquid into the bubble interior. This could conceivably cause a bioeffect through mechanical action or deplete the gas reservoir, but probably is most important in that it affects the size distribution of bubbles in the population, which can affect the type of cavitational behaviour they undertake. The most important such behaviour, which depends on the equilibrium bubble size, is the phenomenon of 'inertial cavitation' (formerly known as 'transient cavitation'). This will now be described.

When bubbles within a certain size range are driven strongly, they undergo a dramatic change in behaviour (Leighton, 1994, §4.2, §4.3). This transition from non-inertial to inertial cavitation (where the bubble undergoes rapid explosive growth, followed by a violent collapse, generating high gas temperatures, gas shocks, and liquid shocks) is a threshold phenomenon with respect to initial bubble radius, acoustic frequency, and acoustic pressure amplitude. Both the high gas temperatures and the gas shocks may generate free radicals (e.g. in aqueous solution, H atoms, OH radicals, and products such as  $\text{H}_2\text{O}_2$ , hydrogen peroxide). These are highly reactive and may represent a hazard (they are the sources of sonochemical reaction and of sonoluminescence). As regards the hot-spot itself, although its temperature is high, it does not contain significant energy or last for a long time. The *rebound pressure pulse* emitted into the liquid as the bubble rebounds from minimum size may cause mechanical damage to structures close to it (pressure amplitude falls off as  $r^{-1}$  since it is spherically diverging – section 7.2.2.4(a). However in a cloud of bubbles the shocks may act to greater distances through a co-operation effect between many bubbles (cloud concentration).

The threshold is such that there is a critical size range, which increases with increasing acoustic pressure amplitude and decreasing frequency, over which bubbles will undergo inertial/transient collapse if insonated by an appropriate sound field. This is because bubbles which are initially too large, though they will grow sufficiently, are then too sluggish to undergo a collapse that is sufficiently violent. Conversely very small bubbles are prevented from undergoing the initial explosive growth by the Laplace pressure (which increases rapidly with decreasing radius – section 7.2.3.1(b)). Therefore only bubbles of intermediate size will undergo transient collapse. This is illustrated in Fig. 7.33.

Erosion through violent cavitation collapse has been known for many years. One of the earliest observations was of ‘pitting’ in ship propellers. One cause of this is the rebound pressure pulse, which also generates noise. Submariners know that submerging will tend to reduce cavitation noise by suppressing the propeller cavitation. However, when the cavitation is strong

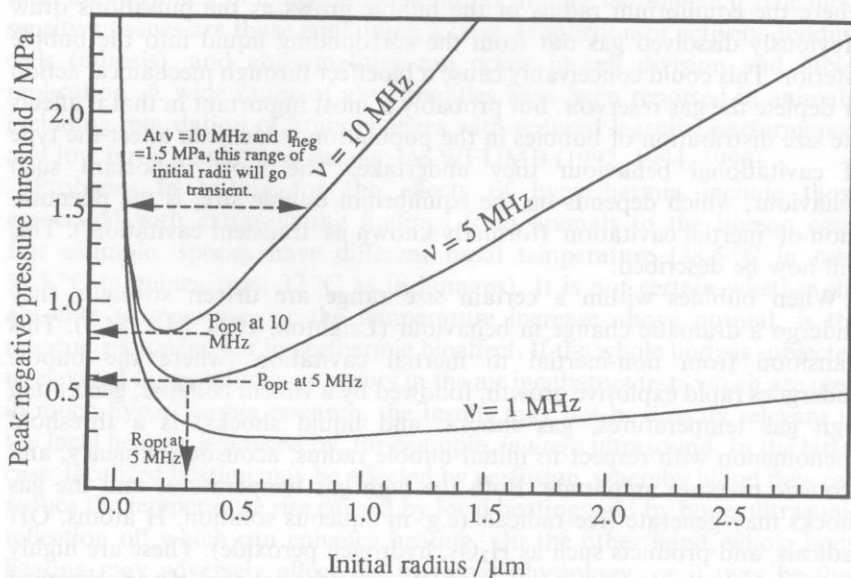


**Figure 7.33** Illustration of the threshold for inertial cavitation, after the calculation of Apfel and Holland (1991), in terms of the variation in the peak negative pressure required to generate inertial cavitation from a free-floating spherical gas bubble nucleus, as a function of the initial radius of that bubble. Above the curve, inertial cavitation will occur. As the acoustic frequency increases, the threshold tends to increase for all initial bubble sizes, and the radius range which will nucleate inertial cavitation decreases. Reprinted by permission of Elsevier Science from *Ultrasound in Medicine and Biology*, 17, 179–85; copyright © 1991 by World Federation of Ultrasound in Medicine and Biology.



and the vessel is at high speed, increasing the depth of the vessel will first cause an increase in the cavitation noise, before suppression occurs. This so-called 'anomalous depth effect' is due to the fact that an increasing static pressure tends to increase the violence of each individual collapse before, at the highest static pressures, it suppresses the growth phase. However 'pitting' can also be caused by an aspherical form of collapse, which can occur when the bubble is close to an inhomogeneity such as a solid boundary. In such circumstances, the bubble can invert on collapse such that a high-speed liquid jet can pass through the bubble and, on impacting a nearby boundary, can create damage (Leighton, 1994, §5.4.1).

#### *7.4.3.3 Radiation forces*

Direct bioeffects from radiation pressure are not often evident since the magnitude of forces tends to be smaller than, for example, the hydrodynamic stresses induced by bubble activity. A typical diagnostic scanner might generate a pulse average pressure of 1–10 kPa, with a time-average pressure of order 1–10 Pa. This can be compared with the tensile strength of the weakest tissue, which is around 50 kPa (Yamada, 1970). Modest streaming flows of 10 cm/s have been measured in water.

#### **7.4.4 Conclusion**

Which mechanism for bioeffect dominates is dependent on the parameters of a particular sound field. In general, hyperthermia tends to respond to the time-averaged acoustic intensity, since the time-scale of bulk heating is relatively slow. In contrast, bubbles respond almost instantaneously to the acoustic pressure field, so that the question of inertial cavitation will be more dependent on the temporal-peak, rather than the temporal-average, acoustic pressure. Inertial cavitation will not be an issue if one is below the threshold conditions for cavitation. *In vivo* this threshold is likely to be a nucleation threshold; however if nuclei are plentiful, as in aerated water, the relevant threshold is likely to be the one discussed in section 7.4.3.2.

This concluding discussion of the physical acoustic and fluid phenomenon associated with the potential for bioeffect from clinical ultrasound provides a useful exercise for employment of the nonlinear propagation, self-effect, and radiation force considerations given in section 7.3 (Nonlinear underwater acoustics). These in turn benefit from exploitation of the ray path, absorption, and signal-to-noise features introduced in section 7.2 (Ocean acoustics). Similarities do exist between the acoustics of millimetre-wavelength ultrasound in the human body, and sound of much greater wavelengths in the oceans.

## 7.5 REFERENCES

- AIUM (1988) Bioeffects considerations for the safety of diagnostic ultrasound. *J. Ultrasound Med.*, **7**: S1–S38, Supplement no. 9, American Institute of Ultrasound in Medicine, Bioeffects Committee.
- Albers, V. M. (ed.) (1972) *Underwater Sound*, Dowden, Hutchinson, and Ross, Inc., distributed by Academic Press.
- Apfel, R. E. and Holland, C. K. (1991) Gauging the likelihood of cavitation from short-pulse, low-duty cycle diagnostic ultrasound. *Ultrasound Med. Biol.*, **17**, 179–185.
- Baker, A. C. (1991) Prediction of non-linear propagation in water due to diagnostic medical ultrasound equipment. *Phys. Med. Biol.*, **36**, 1457–1464.
- Berkday, H. O. (1965) Possible exploitation of non-linear acoustics in underwater transmitting applications. *J. Sound Vib.*, **2**, 435–461.
- Buckingham, M. (1992) Acoustic daylight: imaging the ocean with ambient noise. *Nature*, **356**, 327–329.
- Buckingham, M. J. and Epifanio, C. L. (1996) Acoustic daylight imaging in the ocean: Experimental Results. In J. Papadakis (ed.) *Proceedings of the 3rd European Conference on Underwater Acoustics (Heraklion, Crete, 24–8 June 1996)*, Crete University Press, Heraklion, 341–347.
- Buckingham, M. J. and Epifanio, C. L. (1997) Bubbles and breaking waves: imaging in space, time and frequency. In T. G. Leighton (ed.) *Natural Physical Processes Associated with Sea Surface Sound*, University of Southampton, 39–44.
- Burdick, W. S. (1984) *Underwater Acoustic System Analysis*, Prentice-Hall, Englewood Cliffs, New Jersey.
- Carey, W. M. (1987) Low-frequency noise and bubble plume oscillations. *J. Acoust. Soc. Am. suppl.* **82**: S62.
- Carstensen, E. L. (1987) Acoustic cavitation and the safety of diagnostic ultrasound. *Ultrasound Med. Biol.*, **13**, 597–606.
- Chen, C-T. and Millero, F. J. (1976) Reevaluation of Wilson's sound-speed measurements for pure water. *J. Acoust. Soc. Am.* **60**, 1270–3.
- Chen, C-T., Fine, R. A. and Millero, F. J. (1977) The equation of state of pure water determined from sound speeds. *J. Chemical Physics*, **66**, 2142–4.
- Clay, C. S. and Medwin, H. (1977) *Acoustical Oceanography*, John Wiley and Sons, New York.
- Coates, R. F. W. (1990) *Underwater Acoustic Systems*, Macmillan, Basingstoke.
- Duck, F. A. and Martin, K. (1991) Trends in diagnostic exposure. *Phys. Med. Biol.* **36**, 1423–32.
- Euler, L. (1759) *Mém. Acad. Sci.* Berlin, **15**, 185–209.
- Finney, R., Halliwell, M., Mishriki, S. F. and Baker, A. C. (1991) Measurement of lithotripsy pulses through biological media. *Phys. Med. Biol.* **36**, 1485–93.
- Fisher, H. and Simmons, V. P. (1977) Sound absorption in sea water. *J. Acoust. Soc. Am.*, **62**, 558.
- Franz, G. J. (1959) Splashes as sources of sound in liquids. *J. Acoust. Soc. Am.* **31**, 1080–1104.
- Fry, F. J., Kossoff, G., Eggleton, R. C. and Dunn, F. (1970) Threshold ultrasonic dosages for structural changes in the mammalian brain. *J. Acoust. Soc. Am.* **48**, 1413–17.
- Jones, A. T. (1920) The sounds of splashes, *Science*, 295–6.
- Kinsler, L. E., Frey, A. R., Coppens, A. B. and Sanders, J. V. (1982) *Fundamentals of Acoustics*, John Wiley and Sons, New York, Ch. 15.

- Knudsen, V. O., Alford, R. S. and Emling, J. W. (1948) Underwater ambient noise. *J. Marine Res.*, **7**, 410–429.
- Langmuir, I. (1938) Surface water motion induced by wind. *Science*, **87**, 119–123.
- Laville, F., Abbott, G. D. and Miller, M. J. (1991) Underwater sound generation by rainfall. *J. Acoust. Soc. Am.* **89**, 715–721.
- Leighton, T. G. (1994) *The Acoustic Bubble*, Academic Press, London.
- Leighton, T. G. (1995) Bubble population phenomena in acoustic cavitation. *Ultrasonics Sonochemistry*, **2**, S123–S136.
- Leighton, T. G., Schneider, M. F. and White, P. R. (1995) Study of bubble fragmentation using optical and acoustical techniques. In M. J. Buckingham and J. R. Potter (eds) *Proceedings of 3rd Meeting on the Natural Physical Processes Related to Sea Surface Sound*, World Scientific Publishing Ltd, Singapore, 414–28.
- Leroy, C. C. (1969) Development of simple equations for accurate and more realistic calculation of the speed of sound in sea water. *J. Acoust. Soc. Am.* **46**, 216.
- Lizzi, F. L., Driller, J., Lunzer, B., Kalisz, A. and Coleman, D. J. (1992) Computer-model of ultrasonic hyperthermia and ablation for ocular tumors using B-mode data. *Ultrasound Med. Biol.*, **18**, 59–73.
- Longuet-Higgins, M. S. (1990) Bubble noise spectra. *J. Acoust. Soc. Am.* **87**, 652–61.
- Longuet-Higgins, M. S. and Turner, J. S. (1974) An 'entraining plume' model of a spilling breaker. *J. Fluid Mech.* **63**, 1–20.
- Lyman, J. and Fleming, R. H. (1940) *J. Mar. Res.* **3**, 134–46.
- Mackenzie, K. V. (1981) Nine-term equation for sound speed in the oceans. *J. Acoust. Soc. Am.* **70**, 807.
- Medwin, H. (1975) Speed of sound in water for realistic parameters. *J. Acoust. Soc. Am.*, **58**, 1318.
- Medwin, H., Kurgan, A. and Nystuen, J. A. (1990) Impact and bubble sound from raindrops at normal and oblique incidence. *J. Acoust. Soc. Am.* **88**, 413–8.
- Mikhalevsky, P. N. and Baggeroer, A. B. (1995) Experiment tests use of acoustics to monitor temperature and ice in Arctic Ocean. *Eos, Trans. Am. Geophys. U.*, **76**, 265.
- Miller, D. L. and Williams, A. R. (1989) Bubble cycling as the explanation of the promotion of ultrasonic cavitation in a rotating tube exposure system. *Ultrasound Med. Biol.* **15**, 641–64.
- Miller, D. L., Nyborg, W. L. and Whitcomb, C. C. (1979) Platelet aggregation induced by ultrasound under specialized condition in vitro. *Science*, **205**, 505.
- Minnaert, M. (1933) On musical air-bubbles and sounds of running water, *Phil. Mag.*, **16**, 235–48.
- Monahan, E. C. and Lu, N. Q. (1990) Acoustically relevant bubble assemblages and their dependence on meteorological parameters. *IEEE J. Oceanic. Eng.*, **15**, 340–5.
- Munk, W. and Baggeroer, A. B. (1994) The Heard Island Papers: a contribution to global acoustics. *J. Acoust. Soc. Am.*, **96**, 2327.
- Nystuen, J. A. (1986) Rainfall measurements using underwater ambient noise. *J. Acoust. Soc. Am.* **79**, 972–982.
- Oğuz, H. N. and Prosperetti, A. (1990) Bubble entrainment by the impact of drops on liquid surfaces. *J. Fluid Mech.*, **219**, 143–179.
- Premus, V. and Spiesberger, J. L. (1997) Can acoustic multipath explain finback (*B. physalus*) 20-Hz doublets in shallow water? *J. Acoust. Soc. Am.*, **101**, 1127–1138.
- Prosperetti, A. (1988) Bubble-related ambient noise in the ocean. *J. Acoust. Soc. Am.* **84**, 1042–54.

- Pumphrey, H. C. (1989) Sources of ambient noise in the ocean: an experimental investigation. PhD Thesis, University of Mississippi.
- Pumphrey, H. C. and Elmore, P. A. (1990) The entrainment of bubbles by drop impacts. *J. Fluid Mech.*, **220**, 539–567.
- Pumphrey, H. C., Crum, L. A. and Bjørnø, L. (1989) Underwater sound produced by individual drop impacts and rainfall. *J. Acoust. Soc. Am.* **85**, 1518–26.
- Richards, S. D., Heathershaw, A. D. and Thorne, P. D. (1996) The effect of suspended particulate matter on sound attenuation in seawater. *J. Acoust. Soc. Am.* **100**, 1447–50.
- Robinson, A. R. (ed.) (1983) *Eddies in Marine Science*. Springer-Verlag, New York.
- Ross, D. (1976) *Mechanisms of Underwater Noise*. Pergamon Press, New York.
- Roy, R. A., Carey, W., Nicholas, M. and Crum, L. A. (1992) Low-frequency scattering from bubble clouds. *Proceedings of 14th International Congress on Acoustics*, Beijing, China.
- Scrimger, J. A., Evans, D. J., McBean, G. A., Farmer, D. M. and Kerman, B. R. (1987) Underwater noise due to rain, hail and snow. *J. Acoust. Soc. Am.* **81**, 79–86.
- Starrit, H. C., Duck, F. A. and Humphrey, V. F. (1989) An experimental investigation of streaming in pulsed diagnostic ultrasound beams. *Ultrasound Med. Biol.*, **15**, 363–73.
- ter Haar, G., Dyson, M. and Oakley, E. M. (1987) The use of ultrasound by physiotherapists in Britain, 1985. *Ultrasound Med. Biol.*, **13**, 659–663.
- ter Haar, G., Rivens, I., Chen, L. and Riddler, S. (1991) High intensity focused ultrasound for the treatment of rat tumours. *Phys. Med. Biol.*, **36**, 1495–1501.
- Thorpe, S. A. (1982) On the clouds of bubbles formed by breaking wind-waves in deep water, and their role in air-sea gas transfer. *Philos. Trans. R. Soc. London, A* **304**, 155–210.
- Thorpe, S. A. (1984) The effect of Langmuir circulation on the distribution of submerged bubbles caused by breaking wind waves. *J. Fluid. Mech.*, **142**, 151–70.
- Thorpe, S. A. (1986) Measurements with an Automatically Recording Inverted Echo Sounder; ARIES and the Bubble Clouds. *J. Phys. Oceanography*, **16**, 1462–78.
- Thorpe, S. A. (1992) Bubble clouds and the dynamics of the upper ocean. *Q. J. Meteorol. Soc.* **118**, 1–22.
- Thorpe, S. A. and Hall AJ. (1980) The mixing layer of Loch Ness. *J. Fluid Mech.*, **101**, 687–703.
- Thorpe, S. A. and Hall AJ. (1983) The characteristics of breaking waves, bubble clouds and near-surface currents observed using side-scan sonar. *Continental Shelf Res.*, **1**, 353–384.
- Tolstoy, I. and Clay, C.S. (1966) *Ocean Acoustics*, McGraw-Hill, New York.
- Urick, R. J. (1983) *Principles of Underwater Sound*, McGraw-Hill, New York.
- Vivino, A. A., Boraker, D. K., Miller, D. and Nyborg, W. (1985) Stable cavitation at low ultrasonic intensities induces cell death and inhibits <sup>3</sup>H-TdR incorporation by con-a-stimulated murine lymphocytes *in vitro*. *Ultrasound Med. Biol.*, **11**, 751–9.
- Webb, D. J., Beckles, D., de Cuevas, B. A. *et al.* (1991) An eddy-resolving model of the Southern Ocean. *Transactions of the American Geophysical Union*, **72**, 169–75.
- Westervelt, P. J. (1960) Parametric end-fire array. *J. Acoust. Soc. Am.*, **32**, 934–5.
- WFUMB (1992) Symposia for Safety and Standardization in Medical Ultrasound: Issues and recommendations regarding thermal mechanisms for biological effects of ultrasound. In S. B. Barnett and G. Kossof (eds), *Ultrasound Med. Biol.*, **18**(9) (Special issue).
- WFUMB (1994, 1996) *Symposia for Safety of Ultrasound in Medicine: Emphasis on non-thermal effects*. World Federation for Ultrasound in Medicine and Biology

- (draft document), Barnett, S. (ed) (Utsunomiya, Japan, 1994; Koster Banz, Germany, 1996).
- Williams, A. R. (1990) Editorial to Bioeffects special issue. *Ultrasonics*, **28**, 131.
- Wunsch, C. (1981). Low frequency variability of the sea. In B. A. Warren and C. Wunsch (eds), *Evolution of Physical Oceanography*, Cambridge, MIT Press, Mass, 342–77.
- Yamada, H. (1970) *Strength of Biological Materials* (F. G. Evans, ed.). Waverley Press, Inc. Baltimore.
- Ziskin, M. C. (1987) The prudent use of diagnostic ultrasound. *J. Ultrasound Med.*, **6**, 415.

## 7.6 QUESTIONS

- 1 (a) A source of sound transmits into the ocean, where  $I_1$  and  $c_1$  are the acoustic intensity and sound speed (respectively) at a distance of 1 metre from the source; and where  $I_2$  and  $c_2$  are the acoustic intensity and sound speed (respectively) at a distant point  $X$ . As a result of ray divergence, there is a certain transmission loss ( $TL$ ), defined as  $TL = 10 \log_{10}(I_1/I_2)$ , between the source and point  $X$ . By considering two rays, which leave the source at angles of  $\theta_1 + \delta\theta/2$  and  $\theta_1 - \delta\theta/2$ , find an expression for the transmission loss in terms of  $\delta\theta$ ,  $c_1$  and  $c_2$ ; the length ( $\delta h$ ) of the vertical line which extends between the two rays and intersects point  $X$ ; and the horizontal distance ( $r$ ) between the source and point  $X$ . Assume no absorption of the acoustic energy by the sea.
- (b) Use Huygens' principle to demonstrate the formation of sound channels at *both* the sea surface *and* at about 1 km depth (the SOFAR channel), indicating the local sound speed profiles that you assume in both cases. State two physical mechanisms by which a surface channel might form, and discuss the relationship between the angle a ray in the SOFAR channel makes with the axis when they intersect, and the travel time taken for a pulse using that ray path to propagate to a long distance. Use your answer to part (a) of this question to demonstrate that spreading losses over large distances (e.g. of order 1000 km) would be less in a sound channel than for spherical spreading.
- (c) Describe how this principle has been exploited in climate monitoring, including a detailed discussion of the initial feasibility study *and* brief outlines of two subsequent experiments.
2. (a) Discuss the production of underwater sound by rain, describing both the contributions from both bubble and non-bubble sources.
- (b) Consider a cubic meter of bubbly water, containing  $V_a = 100 \text{ ml} = 10^{-4} \text{ m}^3$  of gas as bubbles, so that volume of water is  $V_w = 1 - 10^{-4} = 0.9999 \text{ m}^3$ . Compare the quasi-static compression of this water with that of 1 cubic metre of bubble-free water. Hence estimate the change in sound speed which the introduction of such a



- bubble population would induce, were the acoustic frequency so much less than the bubble resonance as to impose quasi-static conditions.
- (c) Strong acoustic backscatter is observed when 400 Hz sonar beams, angled a few degrees from the horizontal, are deployed to examine the sea surface under stormy conditions. Discuss scatter from surface waves, and from bubbles, in this context.
3. (a) Euler's equation in one spatial dimension ( $x$ ) relates the total pressure ( $P$ ) to the particle velocity ( $u$ ) and the liquid density ( $\rho$ ), as a function of time. Combine Euler's equation with the equation of continuity and the wavespeed equation (all three of which can be quoted without proof) to demonstrate, with full working, how the one-dimensional wave equation may be derived. State clearly and precisely all assumptions, and comment on whether each assumption is justified.
  - (b) Use a power-series approximation of the nonlinearity to demonstrate the generation of harmonics during the propagation of an initially sinusoidal acoustic wave in water. Using sketches of the waveforms and associated spectra at various positions from the transducer, discuss how the energy is distributed with respect to frequency, the mechanisms which change this distribution, and the effects on the waveform.
  - (c) Use the same power-series approximation of the nonlinearity associated with propagation to mathematically describe the principle of operation of parametric sonar. Describe the characteristics and advantages of parametric transmitters and receivers.
  - (d) Write the expression relating the phase velocity, the particle velocity ( $u$ ), and the speed of sound for waves of infinitesimal amplitude ( $c_0$ ), for an isentropic gas and for a liquid, introducing a constant based on the nonlinearity parameter,  $B/2A$ , of the liquid, and (for the gas) the equivalent measure of nonlinearity,  $(\gamma - 1)/2$ . Here  $\gamma$  represents the ratio of the specific heat of the gas at constant pressure, to that at constant volume. Since  $B/2A = 2.5$  for water, whereas, for air,  $(\gamma - 1)/2 = 0.2$ , one might therefore expect to see the effects of nonlinear propagation in water more readily than in air. However, often the converse is true. Why is this?
4. (a) Describe how the use of diagnostic ultrasound over the last 30 years in the UK has been influenced by concern over the potential for hyperthermic bioeffect, indicating the limitations of laboratory tests of such an effect.
  - (b) Describe one medical application which exploits ultrasonic cavitation in humans *in vivo*, including specification of the typical acoustic parameters and (by sketching) pulse profile. Indicate any biohazard concerns associated with this procedure.

- (c) Sketch a graph of the inertial cavitation threshold, using realistic values for the acoustic pressure amplitude axis and the initial bubble radius axis, for acoustic frequencies of 1 MHz, 5 MHz and 10 MHz. Describe why, above the threshold, there exists only a limited range of initial bubble sizes which can nucleate inertial cavitation. Extrapolate from this description to explain the 'anomalous depth effect' observed when submariners attempt to suppress propeller cavitation by diving the submarine to greater depths.

---

R. J. PINNINGTON

### 1.1 INTRODUCTION

Before describing the techniques and limitations of experimental methods it is wise to reflect upon the purpose of measurement. The broad aim of scientific enquiry is the understanding of nature, and probably the first persons with sufficient leisure to pursue this extensively lived in towns in the region of the Aegean sea around 600 BC (Russell, 1991). These people made the initial steps in understanding by proposing ideals or theoretical models, simplified by assumptions, to explain their casual observations of the physical world. For a large part, these theories were not put to the test of careful experiment, for there was a widespread belief that theory resided in the perfection of heaven while to handle lowly matter was to consort with evil (Russell, 1991). This view still has its sympathisers.

It was not until the Renaissance period that scientific enquiry was supported by careful experiments leading to what is known as the scientific method. This involves an initial observation and the development of a theory which is tested by an experiment in which the chosen phenomenon is isolated from other contributions; the outcome disproves, confirms or leads to modification to the theory. In summary, theory and experiment are needed as much as a walking man requires two legs.

A theory permits a single phenomenon to be viewed in isolation from all other influences. These influences may be dismissed by the assumptions. The reality of the world, however, is that there is always interaction between everything; it and us are a whole; we are related. To be slightly disturbing, Berkeley (Russell, 1991) thought that an event may not even occur unless perceived by the observer, i.e. the event needs the observer. Implicit in the quantum mechanics view of the universe adopted in the twentieth century is the notion that the presence of the observer will always interfere with the outcome of an event. The objective then of a good experiment is to be